

Apparent dispersion in pulsar braking index measurements caused by timing noise

Andrés F. Vargas^{1,2*}, and Andrew Melatos^{1,2}

¹*School of Physics, University of Melbourne, Parkville, VIC 3010, Australia*

²*OzGrav: The ARC Centre of Excellence for Gravitational-wave Discovery, University of Melbourne, Parkville, VIC 3010, Australia*

Accepted XXX. Received YYY; in original form ZZZ

ABSTRACT

Stochastic temporal wandering of the spin frequency ν of a rotation-powered pulsar (i.e. the achromatic component of timing noise unrelated to interstellar propagation) affects the accuracy with which the secular braking torque can be measured. Observational studies confirm that pulsars with anomalous braking indices $|n| = |\nu\dot{\nu}/\dot{\nu}^2| \gg 1$ exhibit elevated levels of timing noise, where an overdot symbolizes a derivative with respect to time. Here it is shown, through analytic calculations and Monte Carlo simulations involving synthetic data and modern Bayesian timing techniques, that the variance $\langle n^2 \rangle$ of the measured n scales with the square of the timing noise amplitude $\sigma_{\dot{\nu}}$. The anomalous regime $\langle n^2 \rangle \gg 1$ corresponds to $\sigma_{\dot{\nu}}^2 \gg 10^{-60} (\gamma_{\dot{\nu}}/10^{-6} \text{ s}^{-1})^2 (\dot{\nu}/10^{-14} \text{ Hz s}^{-1})^4 (\nu/1 \text{ Hz})^{-2} (T_{\text{obs}}/10^8 \text{ s}) \text{ Hz}^2 \text{ s}^{-5}$, where $\gamma_{\dot{\nu}}$ is a stellar damping time-scale, and T_{obs} is the total observing time. When the inequality in the above condition is reversed, n is dominated by the secular braking torque, and timing measurements return $n \sim 3$, if the secular braking torque is electromagnetic. The variance $\langle n^2 \rangle$ is greater, when the stochastic process driving spin fluctuations differs from the red noise model (e.g. power-law spectral density) assumed in the timing solution.

Key words: methods: data analysis – pulsars: general – stars: rotation

1 INTRODUCTION

The long-term evolution of the braking torque acting on a rotation-powered pulsar offers insights into the physics of the pulsar’s magnetosphere and interior (Blandford & Romani 1988). It can be studied through phase-coherent timing experiments by measuring the braking index,

$$n = \frac{\nu\dot{\nu}}{\dot{\nu}^2}, \quad (1)$$

through measuring pulse arrival times, where $\nu(t)$ is the pulse frequency, and an overdot denotes a derivative with respect to time t . In the special case where the braking torque is proportional to a power of ν , viz. $\dot{\nu} = K\nu^{n_{\text{pl}}}$ with K constant, measurements of pulse arrival times yield $n = n_{\text{pl}}$ in the absence of stochastic fluctuations in $\nu(t)$ of intrinsic or instrumental origin. Physical examples of power-law braking include vacuum magnetic dipole radiation ($n_{\text{pl}} = 3$) (Gunn & Ostriker 1969), vacuum electromagnetic radiation for higher-order multipoles with or without general relativistic corrections ($n_{\text{pl}} > 3$) (Pétri 2015, 2017), an extended corotating dipole magnetosphere ($2 \lesssim n_{\text{pl}} \lesssim 3$) (Melatos 1997) or its multipolar off-centred generalization (Pétri 2015, 2016), mass quadrupole gravitational radiation

($n_{\text{pl}} = 5$) (Thorne 1980), gravitational radiation from r-mode instabilities ($n_{\text{pl}} = 7$) (Papaloizou & Pringle 1978; Andersson 1998; Owen et al. 1998), and the hydromagnetic torque exerted by an approximately force-free electron-position magnetosphere and relativistic wind ($2 \lesssim n_{\text{pl}} \lesssim 3$) (Goldreich 1970; Contopoulos & Spitkovsky 2006; Bucciantini et al. 2006; Kou & Tong 2015).¹ Phase-coherent timing experiments on pulsars that do not involve major corrections for rotational glitches typically return $2 \lesssim n \lesssim 3$, consistent with a braking torque of electromagnetic origin (Livingstone et al. 2007; Livingstone & Kaspi 2011), although there are close exceptions such as PSR J1640–4631 ($n = 3.15 \pm 0.03$) (Archibald et al. 2016). An electromagnetic braking torque is also indicated in some glitching pulsars with high-cadence timing data, e.g. PSR J0534+2200 and PSR J0835–4510, where it is possible to correct for post-glitch recoveries with high accuracy (Lyne et al. 1996; Fuentes et al. 2017; Akbal et al. 2021).

A number of rotation-powered pulsars exist, whose measured braking indices are termed ‘anomalous’, because $|n|$ greatly exceeds the standard electromagnetic value, with $3 \ll |n| \lesssim 10^6$ typi-

¹ It is claimed sometimes that a relativistic wind obeys $n_{\text{pl}} = 1$. This value applies to the split-monopole geometry (Michel & Tucker 1969), a theoretical approximation which cannot be realized physically. A realistic wind launched from a dipole magnetosphere obeys $2 \lesssim n_{\text{pl}} \lesssim 3$ (Blandford & Romani 1988; Arons 1992; Bucciantini et al. 2006; Zhang et al. 2022).

* E-mail: afvargas@student.unimelb.edu.au

cally, and n is negative in some objects (Johnston & Galloway 1999; Chukwude & Chidi Odo 2016; Parthasarathy et al. 2020; Lower et al. 2020). It is hard to identify a plausible physical mechanism described by $\dot{\nu} = K\nu^{n_{\text{pl}}}$ with K constant and $n_{\text{pl}} \sim 10^6$. An alternative is that one has $n_{\text{pl}} \approx 3$, but K evolves on a time-scale τ_K much shorter than the spin-down time-scale, implying $n = n_{\text{pl}} + (\dot{K}/K)(\nu/\dot{\nu}) \approx \nu/(\dot{\nu}\tau_K) \gg n_{\text{pl}}$. Mechanisms include (counter)alignment of the rotation and magnetic axes (Goldreich 1970; Link & Epstein 1997; Melatos 2000; Barsukov et al. 2009; Johnston & Karastergiou 2017), magnetic field evolution due to ohmic dissipation or Hall drift (Tauris & Konar 2001; Geppert & Rheinhardt 2002; Pons et al. 2012; Gourgouliatos & Cumming 2015), and precession (Barsukov & Tsygan 2010; Biryukov et al. 2012; Goglichidze et al. 2015; Wasserman et al. 2022). Another alternative — which is the focus of this paper — is that the deterministic, power-law torque is masked by a stochastic process, which dominates $\dot{\nu}$ over typical observational time-scales. Examples include relaxation processes mediated by crust-superfluid coupling between rotational glitches (Alpar & Baykal 2006; Gügercinoğlu & Alpar 2014; Akbal et al. 2017; Gügercinoğlu 2017; Lower et al. 2021) and red timing noise intrinsic to the rotation of the stellar crust or superfluid core (Cordes & Downs 1985; Alpar et al. 1986; Jones 1990; D’Alessandro et al. 1995; Melatos & Link 2014; Chukwude & Chidi Odo 2016), as distinct from timing noise produced by propagation effects in the magnetosphere and interstellar medium (Goncharov et al. 2021). The stochastic process may mask the deterministic braking physically, by adding a fluctuating component to the torque, or observationally, by confounding the measurement of the long-term temporal average of $\dot{\nu}$, e.g. by contaminating the Taylor coefficients of a polynomial ephemeris (Chukwude et al. 2010; Coles et al. 2011). Several population studies confirm that anomalous braking indices are correlated with glitch activity and timing noise amplitude (Arzoumanian et al. 1994; Johnston & Galloway 1999; Urama et al. 2006; Lower et al. 2021).

In this paper, we quantify further the role played by stochastic timing noise in masking an underlying, secular braking torque. We run a set of controlled, systematic, Monte Carlo simulations, in which pulse times of arrival (TOAs) are generated synthetically for an ensemble of pulsars following $\ddot{\nu}(t) = \ddot{\nu}_{\text{em}}(t) + \zeta(t)$, where $\ddot{\nu}_{\text{em}}(t)$ obeys power-law braking, i.e. $\dot{\nu}_{\text{em}}(t) = K\nu_{\text{em}}^{n_{\text{pl}}}(t)$ with $n_{\text{pl}} = 3$ (say) and K constant, and $\zeta(t)$ is a phenomenological fluctuating driver, whose power spectral density (PSD) can be white or colored. The measured braking index n , defined according to (1), is estimated from the synthetic data by modern Bayesian methods using the software package TEMPONEST (Shannon & Cordes 2010; Lentati et al. 2014; Parthasarathy et al. 2020; Lower et al. 2021). The goals are to quantify (i) the dispersion in n , when n is measured thus in the presence of timing noise, and (ii) the conditions under which one obtains $|n| \gg n_{\text{pl}}$. Quantifying (i) and (ii) is the natural next step in extending previous pioneering work on this topic (Johnston & Galloway 1999; Chukwude 2003; Urama et al. 2006; Chukwude et al. 2010; Biryukov et al. 2012; Chukwude & Chidi Odo 2016; Parthasarathy et al. 2019, 2020; Goncharov et al. 2021; Lower et al. 2021).

The paper is structured as follows. In Section 2 we introduce a simple model to generate noisy time series to emulate TOAs and show how n can be measured with TEMPONEST. In Section 3 we conduct an ensemble of systematic numerical experiments with synthetic data to calculate the probability distribution of measured n values as a function of the strength of the timing noise and other properties of its PSD. In Section 4 and the Appendix, we derive the condition on the noise amplitude that yields $|n| \gg n_{\text{pl}}$ in a population sense. Section

5 summarizes the conclusions. We emphasize that the results in Sections 3 and 4 cannot be deduced from real data, as there is no way at present to predict theoretically from first principles the statistical properties of the stochastic torque in a real pulsar. The properties can only be inferred indirectly from timing data, and the inference exercise itself is conditional on a model for the stochastic torque, just like in Section 2 of this paper. However, as a better understanding develops of the underlying physics of timing noise in the future, there is some prospect that the approach in this paper — with an independent predictive model replacing the one in Section 2 — can be applied to real data to disentangle the stochastic and secular contributions to n in individual pulsars.

2 SIMULATING BRAKING INDEX MEASUREMENTS

The twin goals of the paper are to quantify the dispersion in measurements of n caused by timing noise, and to infer a condition on the noise amplitude that yields $|n| \gg n_{\text{pl}}$. To these ends, we perform the following numerical experiment. (i) We create noisy synthetic time series for the dynamical variables in a typical pulsar timing experiment, namely the pulse phase and its first three time derivatives (up to $\ddot{\nu}$), and convert them into TOAs. (ii) We feed the synthetic TOAs into TEMPO2 (Hobbs et al. 2006) and TEMPONEST (Lentati et al. 2014) to get two independent “traditional” timing solutions. Two solutions are generated instead of one as a cross-check. (iii) We infer the measured value of n from the synthetic timing solutions and compare it with the injected value of n_{pl} . (iv) We repeat steps (i)–(iii) for an ensemble of random realizations of the noise in order to compute the statistics of n .

Section 2 sets out the specific procedures involved in steps (i)–(iv) to assist the interested reader in reproducing the numerical experiment, e.g. to calibrate the interpretation of real data in the future. In Section 2.1 we describe the stochastic model used to generate the synthetic time series. Sections 2.2 and 2.3 explain how to convert the synthetic time series into TOAs and track the dynamical variables respectively. Section 2.4 presents an end-to-end worked example of the entire procedure for an arbitrary but representative synthetic pulsar with the rotational parameters of PSR J0942–5552.

2.1 Deterministic and stochastic torques

The electromagnetic pulses emitted by a rotation-powered pulsar are assumed to be phase-locked to the rigid crust and corotating magnetosphere, as long as the emission region does not drift in longitude, i.e. it is assumed in this paper that there is no random walk in the phase $\phi(t)$, beyond what is inherited from the randomly walking frequency via $\phi(t) = \int_0^t dt' \nu(t')$, cf. Cordes & Helfand (1980). Hence the spin-down evolution is described in general by four independent variables: the rotational phase $\phi(t)$, the rotational frequency $\nu(t)$ of the crust, and its derivatives $\dot{\nu}(t)$ and $\ddot{\nu}(t)$, where an overdot denotes differentiation with respect to time. The dynamical variables are packaged into a column vector $\mathbf{X} = (X_1, X_2, X_3, X_4)^T = (\phi, \nu, \dot{\nu}, \ddot{\nu})^T$, where T denotes the matrix transpose.

The state vector \mathbf{X} evolves under the action of deterministic and stochastic torques. In this paper, the deterministic torque is taken to be the standard magnetic dipole torque, with K constant and $n_{\text{pl}} = 3$ (Gunn & Ostriker 1969), but alternatives like a force-free relativistic wind ($n_{\text{pl}} \approx 3$) (Bucciantini et al. 2006) or mass quadrupole gravitational radiation ($n_{\text{pl}} = 5$) (Thorne 1980) would serve just as well. For

simplicity the stochastic torque is taken phenomenologically to be a white noise Langevin term driving $\ddot{v}(t)$. Here too there exist valid alternatives, which can be accommodated naturally within the mathematical framework below; the reader is encouraged to experiment, as the need arises. The model also allows for noise to be added to a combination of $v(t)$ and/or $\dot{v}(t)$, when astronomical data warrant (Cheng 1987; Jones 1990; Meyers et al. 2021a,b; Antonelli et al. 2022). Importantly, a white noise driver in $\ddot{v}(t)$ produces red noise in the measured variables $\phi(t)$, $v(t)$ and $\dot{v}(t)$, because the white noise is filtered by the damping terms in the Langevin equation. We calibrate the noisy driver to generate phase residuals that resemble qualitatively those observed in real pulsars, as explained in Section 2.4. Satisfactory phase residuals can be achieved for drivers described by a range of functional forms.

The above model is described by a set of four simultaneous stochastic differential (Langevin) equations

$$d\mathbf{X} = (\mathbf{A}\mathbf{X} + \mathbf{E}) dt + \mathbf{\Sigma} d\mathbf{B}(t), \quad (2)$$

with

$$\mathbf{A} = \begin{pmatrix} 0 & 1 & 0 & 0 \\ 0 & -\gamma_v & 1 & 0 \\ 0 & 0 & -\gamma_{\dot{v}} & 1 \\ 0 & 0 & 0 & -\gamma_{\ddot{v}} \end{pmatrix}, \quad (3)$$

$$\mathbf{E} = \begin{pmatrix} 0 \\ \gamma_v v_{\text{em}}(t) \\ \gamma_{\dot{v}} \dot{v}_{\text{em}}(t) \\ \ddot{v}_{\text{em}}(t) + \gamma_{\ddot{v}} \dot{v}_{\text{em}}(t) \end{pmatrix}, \quad (4)$$

and

$$\mathbf{\Sigma} = \text{diag}(0, 0, 0, \sigma_{\ddot{v}}^2). \quad (5)$$

In (2)–(5), the parameters γ_v , $\gamma_{\dot{v}}$, and $\gamma_{\ddot{v}}$ are constant damping coefficients, and $v_{\text{em}}(t)$ is the solution to the deterministic electromagnetic braking law

$$\dot{v}_{\text{em}}(t) = K v_{\text{em}}^{n_{\text{pl}}}(t), \quad (6)$$

with $n_{\text{pl}} \approx 3$. In (2), $d\mathbf{B}(t)$ denotes the infinitesimal increments of a zero-mean, unit-variance, Wiener process.

It is important to emphasize that (2)–(5) are phenomenological equations of motion, in the spirit of previous related work (Meyers et al. 2021a,b; Antonelli et al. 2022). They are not derived from a physical model of timing noise, such as the two-component crust-superfluid model, nor are they unique. Instead, they aim to reproduce qualitatively the observed timing behavior of typical pulsars, namely that $v(t) \approx v_{\text{em}}(t)$ and $\dot{v}(t) \approx \dot{v}_{\text{em}}(t)$ adhere closely to the secular evolution described by (6), with minimal wandering, while $\ddot{v}(t)$ wanders randomly and significantly around the secular trend $\langle \ddot{v}(t) \rangle = \ddot{v}_{\text{em}}(t)$. One can see this by writing out the second row of (2) explicitly as one example:

$$\frac{dv(t)}{dt} = -\gamma_v [v(t) - v_{\text{em}}(t)] + \dot{v}(t). \quad (7)$$

It is plain that (7) describes a relaxation process, in which $v(t)$ reverts to the mean $v_{\text{em}}(t)$ on a time-scale γ_v^{-1} . The process is driven by the stochastic torque \dot{v} , which inherits its randomness from integration of the white-noise driver with amplitude $\sigma_{\dot{v}}$ in (5). The fluctuations $|v(t) - v_{\text{em}}(t)|$ are small compared to $v_{\text{em}}(t)$, provided that $\gamma_v^2 v_{\text{em}}^2$ is large compared to $\text{var}(\dot{v})$, the variance of \dot{v} , a condition which is always observed to hold astrophysically.

The stochastic torques in the components of the Wiener increment $d\mathbf{B}(t)$ are treated as memory-less, white-noise processes with

$$\langle d\mathbf{B}(t) \rangle = 0, \quad (8)$$

and

$$\langle d\mathbf{B}_i(t) d\mathbf{B}_j(t') \rangle = \mathbf{\Sigma}_{ij} \delta(t - t') \quad (9)$$

where $\langle \dots \rangle$ denotes the ensemble average and $\mathbf{\Sigma}_{ij}$ denotes the (i, j) -th element of (5). We assume zero cross-correlations for simplicity, with $\mathbf{\Sigma}_{ij} = 0$ for $i \neq j$, although it is easy to include off-diagonal elements in $\mathbf{\Sigma}$ in the future, if warranted by pulsar timing data. We also assume in this paper that the stochastic torque is nonzero for \ddot{v} only, with amplitude $\mathbf{\Sigma}_{44} = \sigma_{\ddot{v}}^2$; that is, the other three diagonal components of $\mathbf{\Sigma}$ vanish. This assumption is made for pragmatic reasons: it ensures that $v(t)$, $\dot{v}(t)$, and $\ddot{v}(t)$ are all differentiable, so that a braking index n can be calculated, and the observationally motivated tests in this paper can be conducted.² The assumption may not always hold physically; magnetospheric fluctuations could make the pulsar beam and hence $\phi(t)$ wander randomly in longitude, for example (which would imply $\mathbf{\Sigma}_{11} \neq 0$), over and above any wandering inherited from fluctuations in $v(t)$. Henceforth, we refer to the timing noise model described by equations (2)–(9) as the Brownian model.

2.2 Synthetic TOAs

We generate synthetic TOAs from numerical solutions of (2)–(6) by generating a sample of times t_i , where the phase component $X_1(t_i) = \phi(t_i)$ equals a fiducial value (zero without loss of generality). Every numerical solution of (2)–(6) corresponds to one random realization of the system. Solving (2)–(6) again with a new random seed produces a different state sequence $\mathbf{X}(t_i)$ and hence a different yet statistically equivalent set of TOAs.

To create the TOAs $\{t_1, \dots, t_{N_{\text{TOA}}}\}$, we start by selecting randomly a set of N_{TOA} reference times $\{t'_1, \dots, t'_{N_{\text{TOA}}}\}$ within the observation interval $0 \leq t \leq T_{\text{obs}}$. Random in this context means selected with uniform probability per unit time in the foregoing interval, i.e. according to a Poisson process. We then integrate (2)–(6) numerically from the desired initial conditions $\mathbf{X}(t_0)$ to obtain $\{\mathbf{X}(t'_1), \dots, \mathbf{X}(t'_{N_{\text{TOA}}})\}$. For each intermediate state $\mathbf{X}(t'_i)$ we record the time shift dt'_i needed to obtain the next zero crossing of the phase, with $X_1(t'_i + dt'_i) = \phi(t'_i + dt'_i) = 0$. The TOAs are then given by

² The Wiener increment, $d\mathbf{B}(t)$, is not differentiable, but its integral $\int_0^t dt' d\mathbf{B}(t')$ is differentiable. As n features derivatives as high as second order, and n is a measurable quantity which must not diverge, one is forced to introduce noise into (2)–(5) “from the bottom up”, i.e. the white noise driver is added to the right-hand side of $d\ddot{v}(t)/dt$ and filtered, through integration, up to $\phi(t)$.

$t_i = t'_i + dt'_i$, and the state vector $\mathbf{X}(t'_i)$ is updated to return $\mathbf{X}(t_i)$ at the i -th TOA. The number of pulses, i.e. the number of times $X_1(t) = \phi(t) = 0$ occurs in the interval $0 \leq t \leq t_i$, is recorded for each TOA t_i . To finish, all TOAs are reported alongside a constant uncertainty Δ_{TOA} .³

The above procedure is implemented in the publicly available *baboo* package.⁴ The code uses the Runge-Kutta Itô integrator found in the *sdeint* python package⁵ to solve (2) numerically (Röbber 2010).

2.3 Bayesian parameter estimation with TEMPONEST

Every synthetic data realization generated via the procedure in Sections 2.1 and 2.2 comprises the initial states $\mathbf{X}(t_0)$, the pulsar's right ascension (RA) and declination (DEC), and the synthetic TOAs $\{t_1, \dots, t_{N_{\text{TOA}}}\}$ with their uncertainties. These data are fed into TEMPO2 (Hobbs et al. 2006) to generate an initial estimate of the parameters $\theta = \{\text{RA}, \text{DEC}, \nu, \dot{\nu}, \ddot{\nu}\}$ and their respective uncertainties $\Delta\theta = \{\Delta\text{RA}, \Delta\text{DEC}, \Delta\nu, \Delta\dot{\nu}, \Delta\ddot{\nu}\}$.

We use the TEMPO2 output for θ to set the priors in TEMPONEST. We assume uniform priors for all five components of θ . The prior range for RA and DEC is $(-10^{-5} \text{ rad}, 10^{-5} \text{ rad})$ around TEMPO2's central estimates. The prior range for ν is $(-10^{-4} \text{ Hz}, 10^{-4} \text{ Hz})$ around TEMPO2's central estimate. For $\dot{\nu}$ we elect to cover the absolute range $(-10^{-12} \text{ Hz s}^{-1}, 0 \text{ Hz s}^{-1})$, as all the synthetic data generated for this paper refer to hypothetical pulsars with $\dot{\nu} \geq -10^{-12} \text{ Hz s}^{-1}$, which are typical of the observed pulsar population (Manchester et al. 2005). For $\ddot{\nu}$ we follow the same approach as in Lower et al. (2020) and Parthasarathy et al. (2020) and cover the range $(-10^3 \Delta\ddot{\nu}, 10^3 \Delta\ddot{\nu})$; the latter range is absolute, it is not centered on TEMPO2's central estimate. We follow the same procedure when analyzing an ensemble of random realizations with fixed $\sigma_{\ddot{\nu}}^2$, as in Sections 3 and 4, except that the prior on $\ddot{\nu}$ spans the range $(-10^3 \langle \Delta\ddot{\nu} \rangle, 10^3 \langle \Delta\ddot{\nu} \rangle)$, where $\langle \Delta\ddot{\nu} \rangle$ is averaged over the ensemble of realizations. The width of the foregoing priors on all five components of θ are characteristic of pulsars in the Australia Telescope National Facility (ATNF) pulsar database (Manchester et al. 2005).

TEMPONEST includes a phenomenological model for the red timing noise in the phase residuals (Lentati et al. 2014). The phase residuals PSD in the frequency domain is given by

$$P_r(f) = \frac{A_{\text{red}}^2}{12\pi^2} \left(\frac{f}{f_{\text{yr}}} \right)^{-\beta}, \quad (10)$$

where A_{red} is the amplitude, β is the spectral index, and we define $f_{\text{yr}} = (1 \text{ year})^{-1}$. We remind the reader that equations (2)–(5) inject white-noise fluctuations into $\ddot{\nu}$ via $\sigma_{\ddot{\nu}}^2$, which are converted into red-noise fluctuations in ϕ , ν and $\dot{\nu}$, when (2)–(5) are integrated, through the high-pass filtering action of the damping terms proportional to γ_ν , $\gamma_{\dot{\nu}}$, and $\gamma_{\ddot{\nu}}$ (Meyers et al. 2021a; Antonelli et al. 2022). Excess white noise in the phase residuals, additional to the red noise in (10), is handled in TEMPONEST by modifying the uncertainties

³ TOAs and their respective measurement uncertainties are reported in neighbouring columns, t_i and $\Delta_{\text{TOA},i}$, in the `.tim` file created by *baboo* (see footnote 4) when generating synthetic data. The uncertainties are processed by TEMPO2 and TEMPONEST when generating an ephemeris. In this paper, when reporting synthetic TOAs, we set $\Delta_{\text{TOA},i} = \Delta_{\text{TOA}}$ for $1 \leq i \leq N_{\text{TOA}}$ for simplicity

⁴ <http://www.github.com/meyers-academic/baboo>

⁵ <https://github.com/mattja/sdeint>

Table 1. Prior ranges for the timing noise parameters used by TEMPONEST.

Parameter [units]	Prior range	Prior type
EFAC	$(-1, 3)$	Uniform
EQUAD [s]	$(10^{-10}, 10^{-2})$	Log-uniform
A_{red} [$\text{yr}^{3/2}$]	$(10^{-15}, 10^{-5})$	Log-uniform
β	$(2, 10)$	Log-uniform

of each TOA according to $\mu = (\text{EQUAD})^2 + (\text{EFAC})\Delta_{\text{TOA}}$, i.e. μ supersedes Δ_{TOA} . Here, EQUAD is the error in quadrature which models stationary excess noise, and EFAC is a fitting factor which corrects for unidentified instrumental effects and imperfect estimates of Δ_{TOA} (Lower et al. 2020). The priors used throughout the paper for the timing noise PSD, EFAC, and EQUAD are summarized in Table 1.

The TEMPONEST estimates of ν , $\dot{\nu}$ and $\ddot{\nu}$ imply a measurement of n via (1). The uncertainties $\Delta\nu$ and $\Delta\dot{\nu}$ are small compared to ν and $\dot{\nu}$, e.g. TEMPONEST yields $\Delta\nu/\nu \sim 10^{-9}$ and $\Delta\dot{\nu}/\dot{\nu} \sim 10^{-3}$ for synthetic data created with $\sigma_{\ddot{\nu}}^2 = 10^{-50} \text{ Hz}^2 \text{ s}^{-5}$. Hence the formal uncertainty in the measured n , denoted by Δn , is dominated by the uncertainty in $\ddot{\nu}$, with

$$\Delta n = \frac{\nu \Delta \ddot{\nu}}{\dot{\nu}^2}. \quad (11)$$

From a random ensemble of synthetic TOA time series, all created for a given $\sigma_{\ddot{\nu}}$, we construct probability distributions of n and Δn following the recipe above. From the distributions, we calculate the average displacement $\text{ERR}(n)$ of the measured n relative to the injected value of n_{pl} . That is, we calculate the average *bias* of the measured braking index relative to n_{pl} .

Of course, $\text{ERR}(n)$ cannot be measured astronomically, because observing a real pulsar involves observing a single noise realization (the real one) instead of an ensemble. There is no way to know where the real noise realization falls within the distribution of possible realizations, and so there is no way to know where the actual n measurement falls within the spread of possible n measurements, let alone where it falls relative to n_{pl} . In order to quantify the spread of possible n measurements, we calculate the average *dispersion* across the ensemble, characterized by the fractional variance

$$\text{DISP}(n) = \frac{\langle n^2 \rangle - n_{\text{pl}}^2}{n_{\text{pl}}^2}. \quad (12)$$

In (12), the average $\langle n^2 \rangle$ is taken over the ensemble of synthetic TOA time series at fixed $\sigma_{\ddot{\nu}}$. $\text{DISP}(n)$ is a key quantity of interest throughout the rest of this paper, because it quantifies the fundamental statistical uncertainty associated with measuring n and n_{pl} in a real pulsar, when only one realization (the real one) is available, and we cannot know where it lies in the ensemble distribution.⁶ It is important to distinguish Δn in (11) and $\text{DISP}(n)$ in (12). The former quantity is the formal uncertainty returned by TEMPO2 or TEMPONEST, when measuring n from a single noise realization, whereas the latter quantity describes the dispersion of outcomes across the ensemble.

⁶ $\text{DISP}(n)$ is crudely analogous to the squared standard error of the sample mean in elementary statistics.

Table 2. Injected rotational parameters and recovered values for the worked example in Section 2.4. Values in parentheses indicate the 1σ uncertainty in the trailing digits. The values of $\nu(t_0)$ and its derivatives are consistent with $n_{\text{pl}} = 3$, whereas the recovered values imply $n = 5248.85 \neq n_{\text{pl}}$. The injected parameters are representative of PSR J0942–5552, an arbitrary but typical pulsar in Lower et al. (2020). The timing analysis assumes the red noise model (10), while the Brownian model (2)–(9) generates the spin fluctuations

. The parameters in the lower half of the table are used to generate the TOA time series.

Parameter	Units	Injected value	Recovered value
$\nu(t_0)$	Hz	1.5051430406	1.5051430479(2)
$\dot{\nu}(t_0)$	$10^{-14} \text{ Hz s}^{-1}$	-5.1380792001	-5.1(1)
$\ddot{\nu}(t_0)$	$10^{-24} \text{ Hz s}^{-2}$	5.23×10^{-3}	9(2)
γ_ν	s^{-1}	1×10^{-13}	–
$\gamma_{\dot{\nu}}$	s^{-1}	1×10^{-13}	–
$\gamma_{\ddot{\nu}}$	s^{-1}	1×10^{-6}	–
$\sigma_{\ddot{\nu}}^2$	$\text{Hz}^2 \text{s}^{-5}$	2.5×10^{-50}	–
T_{obs}	days	1.314×10^3	–
N_{TOA}	–	1.5×10^2	–
Δ_{TOA}	μs	1×10^2	–

2.4 An example: Emulating the representative pulsar PSR J0942–5552

To guide the reader in reproducing the results in this paper, we start with a short worked example. We create a single random realization of synthetic data by solving (2)–(6) for the injected parameters in Table 2, which emulate the arbitrary but representative object PSR J0942–5552 (Lower et al. 2020). The object is chosen because its measured braking index satisfies $n = \nu(t_0)\ddot{\nu}(t_0)/\dot{\nu}(t_0)^2 = 4591.4$, i.e. its observed rotational evolution is dominated by some process other than secular electromagnetic braking with $n = n_{\text{pl}} \approx 3$. The timing noise amplitude $\sigma_{\ddot{\nu}} = 2.5 \times 10^{-50} \text{ Hz}^2 \text{s}^{-5}$ is set in order to make the synthetic phase residuals resemble qualitatively the real phase residuals. In this example, the Brownian model (2)–(9) driving the spin fluctuations differs from the red noise model (10) assumed in the timing analysis.

In Figure 1, we compare visually the synthetic rotational evolution with the actual evolution observed by Lower et al. (2020) in PSR J0942–5552. The aim of the comparison is to check that solving (2)–(9) produces phase residuals and associated rotational dynamics which are realistic astrophysically, in the sense that they resemble the actual observed data from a representative pulsar. The top two panels, viz. Figures 1(a) and 1(b), present the actual and synthetic phase residuals respectively. It is clear visually that the fluctuations in the two plots have similar amplitudes and wandering time-scales. The lower three panels, viz. Figures 1(c)–1(e), display the synthetic evolution of $\nu(t)$, $\dot{\nu}(t)$, and $\ddot{\nu}(t)$ respectively as functions of observing epoch t (in units of MJD). The results are in accord qualitatively with the output of TEMPO2, i.e. $\nu(t)$ is dominated by approximately linear spin down [with $T_{\text{obs}} \ll \nu/(2\dot{\nu})$], $\dot{\nu}$ is approximately constant with fluctuations of fractional amplitude $\sim 10^{-3}$, and $\ddot{\nu}$ fluctuates appreciably about its secular electromagnetic value $\langle \ddot{\nu} \rangle = 5.262 \times 10^{-27} \text{ Hz s}^{-2}$ (corresponding to $n_{\text{pl}} = 3$) with fluctuations of fractional amplitude ~ 1 . These properties are characteristic qualitatively of many of the pulsars timed by Lower et al. (2020). Note that the small fluctuations in $\nu(t)$ and $\dot{\nu}(t)$ are inherited from $\ddot{\nu}(t)$ by integrating the Wiener increments $d\mathbf{B}(t)$ (with $\sigma_{\ddot{\nu}}^2 \neq 0$) in (2), as discussed in Section 2.1, and the larger fluctuations in $\ddot{\nu}(t)$ overwhelm the secular $n_{\text{pl}} = 3$ trend in Figure 1(e).

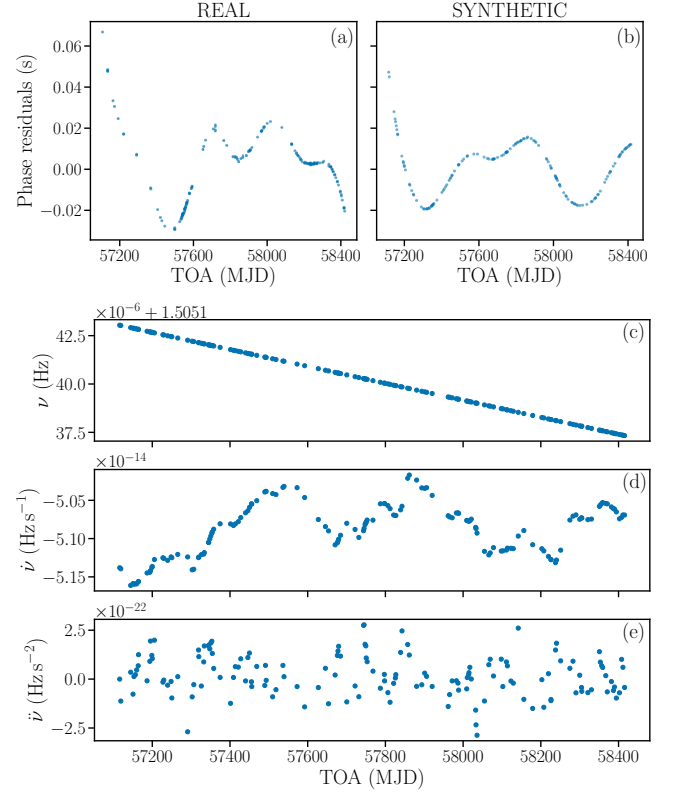


Figure 1. Actual and synthetic rotational evolution of the representative object PSR J0942–5552. (a) Actual phase residuals (units: s) versus observing epoch (units: MJD) taken from Lower et al. (2020). (b) Synthetic phase residuals generated by solving (2)–(6) with the injected parameters in Table 2. The actual and synthetic phase residuals resemble each other visually. (c) Spin frequency $\nu(t)$ (units: Hz) versus observing epoch. (d) $\dot{\nu}(t)$ (units: Hz s^{-1}) versus observing epoch. (e) $\ddot{\nu}(t)$ (units: Hz s^{-2}) versus observing epoch. Note the powers of 10 defining the scales at the top left of panels (c), (d), and (e). Panels (c), (d), and (e) are obtained by solving Equations (2)–(6) with the values listed in Table 2. We set the uncertainties for ν , $\dot{\nu}$, $\ddot{\nu}$ following the procedure detailed in Section 2.3. The fractional fluctuations in panels (c), (d), and (e) are of order $\sim 10^{-8}$, $\sim 10^{-3}$, and ~ 1 respectively, in line with the actual data from PSR J0942–5552.

We feed the synthetic TOAs in Figure 1(b) into TEMPO2 to estimate θ and $\Delta\theta$ in preparation for selecting TEMPNEST priors according to the recipe in Section 2.3. TEMPO2 demands an initial guess for the ephemeris, which we take to be $\mathbf{X}(t_0)$ from Table 2. For the synthetic data in Figure 1(b), TEMPO2 returns $\text{RA} = 2.54051 \text{ rad}$, $\text{DEC} = -0.97532 \text{ rad}$, $\nu = 1.5051 \text{ Hz}$, $\dot{\nu} = -5.0586 \times 10^{-14} \text{ Hz s}^{-1}$ and $\ddot{\nu} = -2.38 \times 10^{-24} \text{ Hz s}^{-2}$, with uncertainties $\Delta \text{RA} = 5.846 \times 10^{-6} \text{ rad}$, $\Delta \text{DEC} = 3.346 \times 10^{-6} \text{ rad}$, $\Delta \nu = 4.7704 \times 10^{-10} \text{ Hz}$, $\Delta \dot{\nu} = 1.9309 \times 10^{-17} \text{ Hz s}^{-1}$ and $\Delta \ddot{\nu} = -3.2965 \times 10^{-25} \text{ Hz s}^{-2}$, implying the priors summarized in Table 3. Except for $\ddot{\nu}$, which is overestimated by $\sim 10^3$, TEMPO2’s estimates for RA, DEC, ν , and $\dot{\nu}$ are close to the injected values, with fractional differences ranging from 10^{-8} to 10^{-2} .

We feed into TEMPNEST the synthetic TOAs from Figure 1(b), as well as the TEMPO2 estimates of θ and the priors in Table 3, to obtain the final estimates for θ , $\Delta\theta$, A_{red} , and β . For this trial the inferred noise parameters are $\log A_{\text{red}} = -9.05 \pm 0.1$, and $\beta = 6.22 \pm 0.4$. These are consistent with the reported values for PSR J0942–5552 in Lower et al. (2020), namely $\log A_{\text{red}} = -9.03 \pm 0.2$, and $\beta = 5.88_{-1.1}^{+1.6}$.

Table 3. Prior ranges set from TEMPO2 estimates of θ and $\Delta\theta$ for the worked example in Section 2.4.

Parameter	Units	Prior range
RA	rad	(2.54050, 2.54052)
DEC	rad	(-0.9753, -0.9751)
ν	Hz	(1.5050, 1.5052)
$\dot{\nu}$	Hz s^{-1}	(-10^{-12} , 0)
$\ddot{\nu}$	$10^{-22} \text{ Hz s}^{-2}$	(-3.3, 3.3)

The values recovered by TEMPONEST for ν , $\dot{\nu}$, and $\ddot{\nu}$ are recorded in the right-hand column of Table 2. The fractional differences between the recovered and injected values are $\sim 10^{-9}$, $\sim 10^{-4}$, and 10^2 for ν , $\dot{\nu}$, and $\ddot{\nu}$ respectively. The recovered parameters in the right column of Table 2, corresponding to the peak of the posterior, are combined through (1) to yield a synthetic measurement of the braking index, viz. $n \pm \Delta n = 5248 \pm 1118$. Here Δn represents the formal uncertainty returned by TEMPONEST when estimating $\Delta \ddot{\nu} = 1.961 \times 10^{-24} \text{ Hz s}^{-2}$. The measurement $n \pm \Delta n$ is consistent with the actual astrophysical value $n = 4591^{+3.1}_{-3.5}$ for PSR J0942–5552 reported by Lower et al. (2020). This is encouraging, when one recalls that the synthetic data are constructed to emulate PSR J0942–5552 and its timing noise parameters.

In the above example, synthetic data are created following the braking law (6) with $n_{\text{pl}} = 3$. Yet timing noise with amplitude $\sigma_{\ddot{\nu}}^2 = 2.5 \times 10^{-50} \text{ Hz}^2 \text{ s}^{-5}$, which matches the observed phase residuals qualitatively and visually [see Figures 1(a) and 1(b)], masks the secular evolution of $\ddot{\nu}$. The synthetic measurement satisfies $n \gg n_{\text{pl}}$. The measured $\Delta \ddot{\nu}$ value is such that the range $n \pm \Delta n$ excludes n_{pl} artificially. In other words, the representative example emulating PSR J0942–5552 demonstrates one instance of the central point of the paper, namely that timing noise can corrupt the inference of n in some pulsars, when the timing noise amplitude takes typical astrophysical values. Having demonstrated the point in principle in one specific example, the logical next step is to test other pulsars with $n \gg n_{\text{pl}}$, e.g. some of the objects studied by Lower et al. (2020). As there is no way at present to measure n_{pl} independently in any real pulsar, we perform Monte Carlo numerical experiments with synthetic data, following the recipe in Section 2.4, to characterize the statistical properties of the recovered braking indices as a function of the injected noise strength $\sigma_{\ddot{\nu}}^2$. These tests and their results form the basis of Sections 3 and 4.

3 STATISTICS OF THE MEASURED BRAKING INDEX

In this section we present the distribution of measured n values returned by TEMPONEST for a range of timing noise amplitudes $\sigma_{\ddot{\nu}}^2$ ranging from relatively low to relatively high, as specified below. The goal is to determine under what conditions n_{pl} is measured reliably via n , i.e. for what values of $\sigma_{\ddot{\nu}}^2$ one obtains $n \approx n_{\text{pl}}$ (low noise) as opposed to $|n| \gg n_{\text{pl}}$ (high noise).

To meet the above goal, we repeat the procedure presented in Section 2.4 using 100 random realizations of synthetic data per $\sigma_{\ddot{\nu}}^2$, as opposed to a single random realization. All the realizations use the same parameters as in Table 2 except for the injected noise strength, which covers the range $10^{-54} \leq \sigma_{\ddot{\nu}}^2 / (1 \text{ Hz}^2 \text{ s}^{-5}) \leq 10^{-50}$. We select this range for $\sigma_{\ddot{\nu}}^2$, because it produces phase residuals consistent with those presented in Lower et al. (2020) and Parthasarathy et al. (2020).

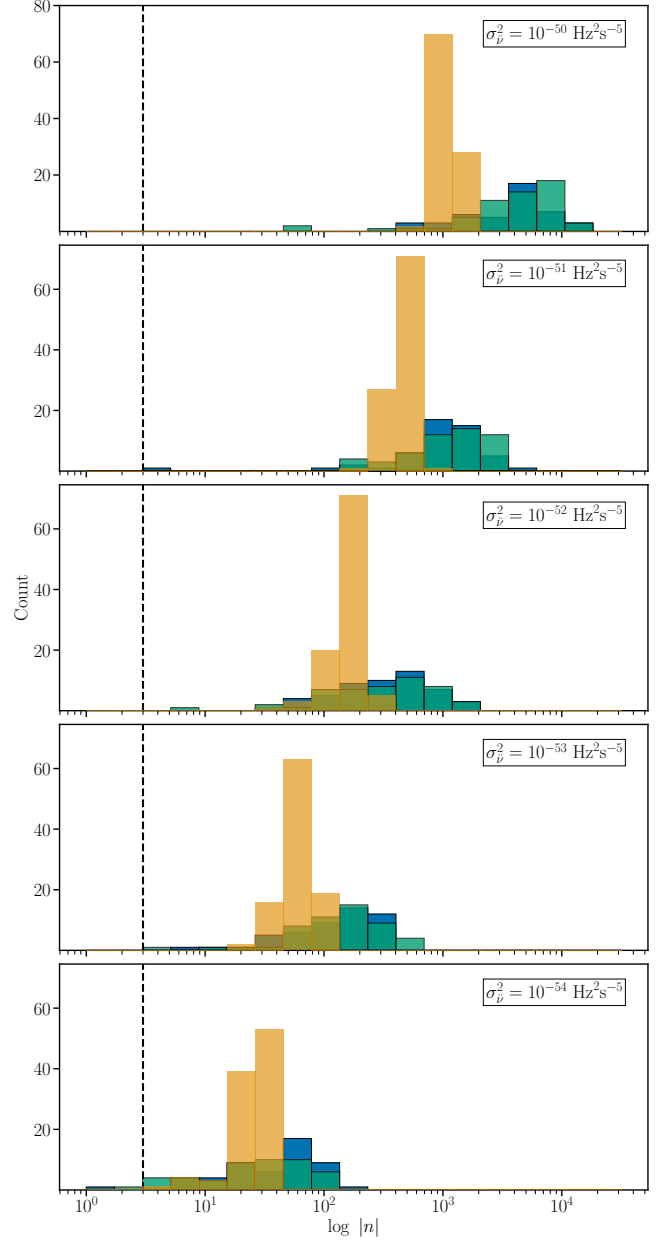


Figure 2. Distribution of n measurements (blue histograms for $n > 0$, cyan histograms for $n < 0$) and their formal uncertainties Δn (orange histograms) reported by TEMPONEST through (1) and (11) for astrophysically plausible timing noise amplitudes running from $\sigma_{\ddot{\nu}}^2 = 10^{-54} \text{ Hz}^2 \text{ s}^{-5}$ in the bottom panel to $\sigma_{\ddot{\nu}}^2 = 10^{-50} \text{ Hz}^2 \text{ s}^{-5}$ in the top panel (see legend). All panels are constructed from 10^2 random realizations of synthetic data at the given $\sigma_{\ddot{\nu}}^2$ and spin parameters characteristic of PSR J0942–5552 from Table 2, noting that the results are approximately independent of $\nu(t_0)$ and $\dot{\nu}(t_0)$ as discussed in Section 4.4. The black dotted line represents the injected value $n_{\text{pl}} = 3$. In the bottom panel the averages of n and Δn are 8 and 26.63 respectively, with the measurements satisfying $n - \Delta n \leq n_{\text{pl}} \leq n + \Delta n$ in 41 out of 100 trials. In the top panel, the averages of n and Δn are -798.73 and 1112.58 respectively, with the measurements satisfying $n - \Delta n \leq n_{\text{pl}} \leq n + \Delta n$ in 8 out of 100 trials. The increase in $\text{DISP}(n)$ from the bottom to the top panel is apparent from the rightward shift of the histograms along the logarithmic horizontal axis.

Specifically, $\sigma_{\dot{\nu}}^2 = 10^{-54} \text{ Hz}^2\text{s}^{-5}$ and $\sigma_{\dot{\nu}}^2 = 10^{-50} \text{ Hz}^2\text{s}^{-5}$ produce phase residuals of order $\sim 10^{-1} \text{ ms}$ and $\sim 10^2 \text{ ms}$, respectively. We set TEMPONEST priors using the same values as in Tables 1 and 3, except for $\dot{\nu}$ whose priors are set following the recipe detailed in Section 2.3. We confirm below (see Section 4.4) that the results for $\text{DISP}(n)$ do not depend on the specific values of ν and $\dot{\nu}$. That is, the results for $\text{DISP}(n)$ obtained for the injection parameters in Table 2 (with only $\dot{\nu}$ and $\sigma_{\dot{\nu}}^2$ varying) transfer approximately unchanged to pulsars with arbitrary ν and $\dot{\nu}$, e.g. in the ATNF database.

Figure 2 demonstrates how the n value measured from (1) becomes less reliable as an estimate of n_{pl} , as the timing noise amplitude $\sigma_{\dot{\nu}}^2$ increases from the bottom panel ($\sigma_{\dot{\nu}}^2 = 10^{-54} \text{ Hz}^2\text{s}^{-5}$) to the top panel ($\sigma_{\dot{\nu}}^2 = 10^{-50} \text{ Hz}^2\text{s}^{-5}$). Each panel displays three histograms. The blue and cyan histograms bin and count the measured $n > 0$ and $n < 0$ values, respectively, as computed from the TEMPONEST output substituted into (1). The orange histogram bins and counts the formal uncertainty Δn reported automatically by TEMPONEST via (11). The histograms are plotted on a logarithmic scale, i.e. $\log_{10} |n|$, for clarity. We observe two things. First, the orange histograms are narrower than the blue and cyan histograms for $\sigma_{\dot{\nu}}^2 \gtrsim 10^{-54} \text{ Hz}^2\text{s}^{-5}$. For example, the full widths half maximum (FWHMs) of the orange and the summed blue and cyan histograms are 16.11 and 89.36 respectively at $\sigma_{\dot{\nu}}^2 = 10^{-54} \text{ Hz}^2\text{s}^{-5}$ and rise to 235.38 and 14932 respectively at $\sigma_{\dot{\nu}}^2 = 10^{-50} \text{ Hz}^2\text{s}^{-5}$. This means that the formal uncertainty on n , as calculated by (11), underestimates the dispersion in n values associated with different random realizations of the timing noise, bearing in mind that timing observations of a real pulsar sample one out of the ensemble of possible realizations, and there is no way to know or predict which one. Second, the FWHMs of the summed blue and cyan histograms are wider than n_{pl} under a range of conditions. For example, the FWHM rises from $29.78 n_{\text{pl}}$ at $\sigma_{\dot{\nu}}^2 = 10^{-54} \text{ Hz}^2\text{s}^{-5}$ to $4977 n_{\text{pl}}$ at $\sigma_{\dot{\nu}}^2 = 10^{-50} \text{ Hz}^2\text{s}^{-5}$. Similarly, $\text{ERR}(n)$ rises from $\text{ERR}(n) = -17.61$ at $\sigma_{\dot{\nu}}^2 = 10^{-54} \text{ Hz}^2\text{s}^{-5}$ to $\text{ERR}(n) = -801.73$ at $\sigma_{\dot{\nu}}^2 = 10^{-50} \text{ Hz}^2\text{s}^{-5}$. Indeed, TEMPONEST routinely returns n values of either sign for $\sigma_{\dot{\nu}}^2 \gtrsim 10^{-54} \text{ Hz}^2\text{s}^{-5}$, in line with many observational studies (Johnston & Galloway 1999; Chukwude & Chidi Odo 2016; Parthasarathy et al. 2020; Lower et al. 2020). This means that the n measurements generated by combining the TEMPONEST output with (1) are unreliable measurements of n_{pl} for $\sigma_{\dot{\nu}}^2 \gtrsim 10^{-54} \text{ Hz}^2\text{s}^{-5}$, noting again that it is impossible to know or predict which random noise realization out of the ensemble of possibilities is sampled by timing observations of any particular real pulsar.

Let us look at the results in Figure 2 in another, equivalent way. As $\sigma_{\dot{\nu}}^2$ increases, fewer of the 10^2 individual trial measurements in the ensemble agree with n_{pl} within the formal uncertainty reported by TEMPONEST. In the bottom panel, for example, only 41 out of 100 trials satisfy $n - \Delta n \leq n_{\text{pl}} \leq n + \Delta n$. For the rest of the panels, in ascending order, only 18, 27, 17, and 8 of the 100 trials satisfy $n - \Delta n \leq n_{\text{pl}} \leq n + \Delta n$.⁷ In other words, as the timing noise amplitude increases, the confidence interval $n \pm \Delta n$ reported by TEMPONEST excludes n_{pl} in more realizations. This result is not surprising. A random noise process corrupts the measurement of an underlying secular trend if it is strong enough; the question is how strong, and the answer here is $\sigma_{\dot{\nu}}^2 \gtrsim 10^{-54} \text{ Hz}^2\text{s}^{-5}$ for the parameters in Table 2, which are

⁷ The non-monotonic order for $\sigma = 10^{-54} \text{ Hz}^2\text{s}^{-5}$ and $10^{-53} \text{ Hz}^2\text{s}^{-5}$ seems to be a statistical fluctuation. It may be checked using an ensemble containing more than 100 trials, when sufficient computational resources become available.

broadly characteristic of known pulsars, e.g. objects in the ATNF database (Lower et al. 2020; Parthasarathy et al. 2020). For example, the top panel in Figure 2 is not extreme. It represents an astrophysically motivated timing noise amplitude, viz. $\sigma_{\dot{\nu}}^2 = 10^{-50} \text{ Hz}^2\text{s}^{-5}$, which produces phase residuals whose variations are comparable to those presented in Figure 2 of Lower et al. (2020), Figure 4 of Parthasarathy et al. (2020) or Figures 1(a) and 1(b) in this paper. The histogram in this panel yields $\langle n \rangle = -798.73$, $\text{max}(n) = 17163$, $\text{ERR}(n) = -801.73$, and $\text{max}(\Delta n) = 1655.8$.

It may be argued that individual trial measurements of n in the histograms in Figure 2 are scattered widely relative to n_{pl} , but the peak of the histogram matches n_{pl} accurately. There are two responses to this argument. First, one never has the opportunity to construct the blue and cyan histograms in Figure 2 when observing a real pulsar. One observes a single random realization of the timing noise – the actual realization – without any way to predict where it lies within the histogram (and therefore where it lies relative to n_{pl}). If there are physical reasons to think that n_{pl} is the same in every pulsar, one could construct the blue and cyan histograms in principle by measuring n in different pulsars. However, existing measurements of nonanomalous braking indices in low-noise pulsars, e.g. the Crab pulsar or PSR J1640–4631, suggest that n_{pl} satisfies $1 \leq n_{\text{pl}} \leq 3$ and may conceivably span an even wider range (Lyne et al. 1993; Archibald et al. 2016). Another possible strategy is to construct the two-dimensional histogram in the n – $\sigma_{\dot{\nu}}^2$ plane for multiple observed pulsars. This strategy might shed some light on the distribution in a population sense. We expand on this point in Sections 4.4 and 5. The second response is that even the peak of the summed blue and cyan histograms does not match n_{pl} accurately. For example, in the top panel of Figure 2, with $\sigma_{\dot{\nu}}^2 = 10^{-50} \text{ Hz}^2\text{s}^{-5}$, the mean and median of the 10^2 trials are -798.73 and -1561.9 respectively, compared to $n_{\text{pl}} = 3$. Generally speaking, TEMPONEST overestimates $|\dot{\nu}|$ on average over the ensemble of trials and underestimates $\Delta \dot{\nu}$.

4 DISPERSION OF MEASURED BRAKING INDICES VERSUS TIMING NOISE PROPERTIES

In this section we calculate the spread of n measurements as a function of $\sigma_{\dot{\nu}}^2$. The aim is to quantify the condition on the noise amplitude that produces $|n| \gg n_{\text{pl}}$ in a probabilistic sense, when one noise realization out of a random ensemble is measured, as in real pulsar timing experiments. To this end, Section 4.1 calculates the dispersion $\text{DISP}(n)$ versus $\sigma_{\dot{\nu}}^2$, using synthetic data with PSR J0942–5552-like values, to find a condition on $\sigma_{\dot{\nu}}^2$ that yields $\text{DISP}(n) \gg 1$. Section 4.2 calculates $\text{DISP}(n)$ as a function of the amplitude and shape of the PSD phase residuals, i.e. the parameters A_{red} and β respectively in equation (10). For the sake of completeness, Section 4.3 calculates the bias $\text{ERR}(n)$ versus $\sigma_{\dot{\nu}}^2$, even though $\text{ERR}(n)$ is not relevant directly to astronomical measurements for the reasons given following equation (11). Section 4.4 calculates $\text{DISP}(n)$ for various values of $\nu(t_0)$ and $\dot{\nu}(t_0)$, holding $\dot{\nu}(t_0)$ and n_{pl} fixed, to verify that $\text{DISP}(n)$ does not depend strongly on $\nu(t_0)$ and $\dot{\nu}(t_0)$. Hence the results in this paper can be applied to any object in the ATNF pulsar database Manchester et al. (2005) without adjusting significantly for $\nu(t_0)$ and $\dot{\nu}(t_0)$.

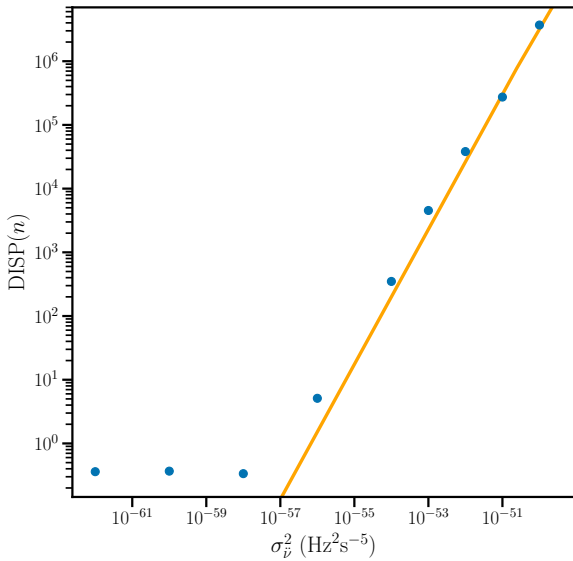


Figure 3. Dispersion $\text{DISP}(n)$ (vertical axis) versus $\sigma_{\dot{\nu}}^2$ (horizontal axis). Each point represent $\text{DISP}(n)$ for 100 synthetic data realizations. We repeat the procedure detailed in Section 2.4 to obtain synthetic n measurements to calculate $\text{DISP}(n)$. The thick solid line represents $\text{DISP}(n)$ as predicted by the analytic theory in Appendix A, when $\dot{\nu}(t)$ is measured nonlocally by finite differencing the time series $\dot{\nu}(t)$. The orange line is a falsifiable prediction from first principles; it is not a fit. For low timing noise strengths (the leftmost three points) we find $\text{DISP}(n) \approx 0.4$ and more than 90% of the recovered $n \pm \Delta n$ intervals include n_{pl} , where Δn is the formal uncertainty returned by TEMPONEST via (11). $\text{DISP}(n)$ grows approximately quadratically with $\sigma_{\dot{\nu}}$ for $\sigma_{\dot{\nu}}^2 \gtrsim 10^{-57} \text{ Hz}^2 \text{ s}^{-5}$. For $\sigma_{\dot{\nu}}^2 = 10^{-50} \text{ Hz}^2 \text{ s}^{-5}$ only 8% of the trials yield $n \pm \Delta n$ intervals that include n_{pl} . The formal uncertainty interval $n \pm \Delta n$ excludes n_{pl} more often, as $\sigma_{\dot{\nu}}^2$ increases.

4.1 $\text{DISP}(n)$ versus $\sigma_{\dot{\nu}}^2$

To explore $\text{DISP}(n)$ versus $\sigma_{\dot{\nu}}^2$, we apply the same numerical recipe outlined in Section 3 to the extended range $10^{-62} \leq \sigma_{\dot{\nu}}^2 / (1 \text{ Hz}^2 \text{ s}^{-5}) \leq 10^{-50}$. Figure 3 displays $\text{DISP}(n)$ (vertical axis), calculated using (12) and n measured from 100 synthetic data realizations, versus the timing noise amplitude, $\sigma_{\dot{\nu}}^2$. The blue dots are obtained from numerical simulations; the orange line is a theoretical prediction discussed further below in this section and Appendix A. Figure 3 reveals two distinct regimes: (i) a flat region with $\text{DISP}(n) \approx 0.4$, spanning $10^{-62} \leq \sigma_{\dot{\nu}}^2 / (1 \text{ Hz}^2 \text{ s}^{-5}) \leq 10^{-58}$, and (ii) a linear region with $0.4 \leq \text{DISP}(n) \leq 4 \times 10^6$, spanning $10^{-58} \leq \sigma_{\dot{\nu}}^2 / (1 \text{ Hz}^2 \text{ s}^{-5}) \leq 10^{-50}$.

In region (i) in Figure 3, TEMPONEST recovers accurately the secular value of $\dot{\nu}(t_0)$, as well as $\nu(t_0)$ and $\dot{\nu}(t_0)$ of course, and therefore returns a reliable estimate of the secular braking index n_{pl} via (1). The number of measured $n \pm \Delta n$ uncertainty intervals that include n_{pl} are 95, 97, and 93 out of 100, for $\sigma_{\dot{\nu}}^2$ values of $10^{-62} \text{ Hz}^2 \text{ s}^{-5}$, $10^{-60} \text{ Hz}^2 \text{ s}^{-5}$, and $10^{-58} \text{ Hz}^2 \text{ s}^{-5}$ respectively. In other words, the evolution of $\dot{\nu}$ is predominantly secular [$\dot{\nu}(t) \approx \dot{\nu}_{\text{em}}(t)$] with negligible contributions from the noise in $\dot{\nu}$. For comparison, in region (i), $\dot{\nu}$ has fluctuations of fractional amplitude $\sim 10^{-6}$, while in Section 2.4 these fluctuations are 10^3 times bigger.

In region (ii) in Figure 3, where we find $\text{DISP}(n) \propto \sigma_{\dot{\nu}}^2$, the spread (standard deviation) of measured n values spans $7.5 \times 10^{-1} \leq (\langle n^2 \rangle - n_{\text{pl}}^2)^{1/2} \leq 6.4 \times 10^2$ for the blue dots. As expected, higher timing noise creates a greater spread in n , with $|n| \geq n_{\text{pl}}$ for $\sigma_{\dot{\nu}}^2 \geq 10^{-54} \text{ Hz}^2 \text{ s}^{-5}$. In region (ii), the number of measured $n \pm \Delta n$ uncertainty intervals that include n_{pl} are 50, 41, 18, 27, 17, and 8 out of 100, for $\sigma_{\dot{\nu}}^2 / (1 \text{ Hz}^2 \text{ s}^{-5})$ equaling 10^{-56} , 10^{-54} , 10^{-53} , 10^{-52} , 10^{-51} , and 10^{-50} respectively. In region (ii), $\dot{\nu}$ exhibits fluctuations of fractional amplitude ~ 1 , and the evolution of $\dot{\nu}(t)$ is mainly driven by the noise term, viz. $\dot{\nu} \approx \int dt' \ddot{\nu}(t')$, instead of $\dot{\nu}_{\text{em}}(t)$. Note that the demarcation point between regions (i) and (ii) depends on exactly how the analyst wishes to define a reliable measurement of n_{pl} . Is it that $\text{DISP}(n)$ falls below some analyst-selected threshold, or is it that the probability of $n \pm \Delta n$ including n_{pl} exceeds some threshold? Both criteria are related and similar, but they are not exactly the same. For instance, $\sigma_{\dot{\nu}}^2 = 10^{-56} \text{ Hz}^2 \text{ s}^{-5}$ yields $[\dot{\nu}(t) - \dot{\nu}_{\text{em}}(t)]/\dot{\nu} = 0.77$, $\text{DISP}(n) = 5.11$, and $\max(n) = 19.15$, but only half of the measured $n \pm \Delta n$ intervals contain n_{pl} . By contrast, $\sigma_{\dot{\nu}}^2 = 10^{-58} \text{ Hz}^2 \text{ s}^{-5}$ yields $[\dot{\nu}(t) - \dot{\nu}_{\text{em}}(t)]/\dot{\nu} = 0.58$, $\text{DISP}(n) = 0.34$, and $\max(n) = 7.75$, but 93 out of the 100 measured $n \pm \Delta n$ intervals contain n_{pl} .

One might wonder whether it is possible to predict the scaling in Figure 3 theoretically. The answer is yes. In Appendix A the Brownian model (2)–(9) is solved analytically in the regime where one has $\nu(t) \approx \nu_{\text{em}}(t)$ but $\dot{\nu}(t)$ fluctuates appreciably about $\dot{\nu}_{\text{em}}(t)$, which is relevant to pulsar timing experiments. The solutions are applied to calculate $\text{DISP}(n)$ via (12) and the result is

$$\text{DISP}(n) = \frac{\sigma_{\dot{\nu}}^2}{\gamma_{\dot{\nu}}^2 \dot{\nu}_{\text{em}}^2(t_0) T_{\text{obs}}} \quad (13)$$

Equation (13) is a central result of the paper. It is drawn as the orange, diagonal line in Figure 3. We emphasize that it is not a best fit, nor is it a phenomenological formula. Rather, it is a falsifiable, analytic result derived from first principles by solving (2)–(9) and calculating $\dot{\nu}$ and hence n by finite differencing the time series $\dot{\nu}(t)$. (Alternative measurement strategies are discussed in Appendix A.) The agreement between the blue dots and orange line in Figure 3, assuming the known, injected values of $\gamma_{\dot{\nu}}$ and $\sigma_{\dot{\nu}}$, is encouraging and confirms the validity of the synthetic measurement strategy involving TEMPONEST. Now that (13) is verified, it can be applied to real astronomical data, by substituting an estimate of $\sigma_{\dot{\nu}}$ from TEMPONEST measurements of $P_r(f)$ (see Section 4.2), and assuming a fiducial value of $\gamma_{\dot{\nu}} \sim 10^{-6} \text{ s}^{-1}$ motivated by pulsar glitch recovery time-scales or the autocorrelation time-scale of pulsar timing noise (Price et al. 2012; Meyers et al. 2021a,b), as well as $\dot{\nu}_{\text{em}}(t_0) \sim \dot{\nu}(t_0)^2 / \nu(t_0)$. In other words, even without knowing $\gamma_{\dot{\nu}}$ and $\sigma_{\dot{\nu}}$ exactly a priori in a real pulsar, one can use (13) to predict approximately the degree to which timing noise masks n_{pl} .

Region (i) in Figure 3 does not obey the trend in (13). The departure is expected. The theory in Appendix A does not describe the complicated instrumental uncertainties embedded in a TEMPONEST measurement, e.g. quantified by Δn and EFAC and EQUAD in Table 1. In other words, in region (i), $\text{DISP}(n)$ is dominated by instrumental uncertainties rather than the randomness of noise realizations. Fortunately, the breakdown of the theory in Appendix A does not matter in practical terms, because we find $\text{DISP}(n) \lesssim 1$ and $n \approx n_{\text{pl}}$ in region (i). That is, wherever instrumental uncertainties are the limiting factor, TEMPONEST measurements of n recover $n_{\text{pl}} \approx n$ accurately anyway.

4.2 DISP(n) versus TEMPONEST phase residual spectrum

Equation (13) involves $\sigma_{\dot{\nu}}^2$, whose exact value is unknown a priori in any real pulsar. However, it is possible to measure $\sigma_{\dot{\nu}}^2$ approximately by relating it to the parameters A_{red} and β in (10) describing the amplitude and shape respectively of the phase residual PSD $P_r(f)$ inferred by TEMPONEST (Lentati et al. 2014, 2016; Goncharov et al. 2021).

Figure 4 serves as a bridge between $\sigma_{\dot{\nu}}^2$, A_{red} and β . For each of the 100 noise realizations analyzed in Section 4.1, we plot a round dot in Figure 4, whose position in the plane of the plot indicates the ordered pair (A_{red}, β) inferred by TEMPONEST, and whose color indicates $\sigma_{\dot{\nu}}^2$ injected in the range $10^{-62} \leq \sigma_{\dot{\nu}}^2 / (1 \text{ Hz}^2 \text{ s}^{-5}) \leq 10^{-50}$. For each of the nine ensembles at fixed $\sigma_{\dot{\nu}}^2 / (1 \text{ Hz}^2 \text{ s}^{-5}) = 10^{-50}, 10^{-51}, 10^{-52}, 10^{-53}, 10^{-54}, 10^{-56}, 10^{-58}, 10^{-60}$, and 10^{-62} (containing 100 random realizations each), we also plot the ensemble averages $\langle A_{\text{red}} \rangle$ and $\langle \beta \rangle$ as open stars, with the enclosed colored dot indicating $\sigma_{\dot{\nu}}^2$ via the color bar. For high timing noise ($\sigma_{\dot{\nu}}^2 \gtrsim 10^{-51} \text{ Hz}^2 \text{ s}^{-5}$), both A_{red} and β are clustered, spanning $\sim 4.2 \text{ yr}^{3/2}$ in A_{red} and $4.5 \lesssim \beta \lesssim 6.9$. The clustering weakens, as $\sigma_{\dot{\nu}}^2$ decreases. For example, for $\sigma_{\dot{\nu}}^2 = 10^{-56} \text{ Hz}^2 \text{ s}^{-5}$, A_{red} and β span $\sim 15 \text{ yr}^{3/2}$ and $2.1 \lesssim \beta \lesssim 9.7$. It means that random variation between noise realizations produces considerable dispersion in A_{red} and β , even when the injected Langevin parameters $\gamma_{\dot{\nu}}$ and $\sigma_{\dot{\nu}}^2$ are the same. In other words, there is a limit to how accurately one can tie TEMPONEST measurements of A_{red} and β to the dynamical parameters of an underlying noise process, whether the process takes the form (2)–(9) or something else. The stars in Figure 4 exhibit a tighter trend, but they are not useful in practical astronomical applications, because one observes a particular noise realization (the actual one) in any given pulsar, with no way of knowing where that realization lies compared to the ensemble average (see Section 3).

The diagonal white band in Figure 4, roughly described by the line $\beta \approx -3.5 \log(A_{\text{red}} / \text{yr}^{3/2}) - 39$, coincides with the demarcation point between region (i) and region (ii), for a PSR J0942–5552-like object. We stress that Figure 4 is representative of PSR J0942–5552-like values and should be reverified with different $\nu(t_0)$ and $\dot{\nu}(t_0)$ when the time comes to apply the controlled synthetic experiments in this paper to a set of real pulsars (see also Section 4.4).

4.3 ERR(n) versus $\sigma_{\dot{\nu}}^2$

As explained in Section 3, it is impossible to construct the blue and cyan histograms, presented in Figure 2, for a real pulsar as only one unique noise realization is measured. Knowing ERR(n) theoretically, therefore, does not help when seeking to predict how far the measured n is displaced from n_{pl} . Instead, DISP(n) is a better proxy. For completeness, we note briefly that ERR(n) increases with $\sigma_{\dot{\nu}}^2$. In region (i) from Figure 3, we find $|\text{ERR}(n)| \leq 0.1$. In region (ii) we find $|\text{ERR}(n)| \approx 0.8$ ($\sigma_{\dot{\nu}}^2 / 10^{-56} \text{ Hz}^2 \text{ s}^{-5}$).

4.4 DISP(n) versus $\nu(t_0)$ and $\dot{\nu}(t_0)$

A natural question is whether or not the results in Sections 3 and 4.1–4.3 depend on $\nu(t_0)$ and $\dot{\nu}(t_0)$. In other words, is it possible to find a universal condition on the noise amplitude that yields $|n| \gg n_{\text{pl}}$ across a large subset of the radio pulsar population, e.g. for a large percentage of the objects in the ATNF Pulsar Database (Manchester et al. 2005; Parthasarathy et al. 2019; Lower et al. 2020; Parthasarathy

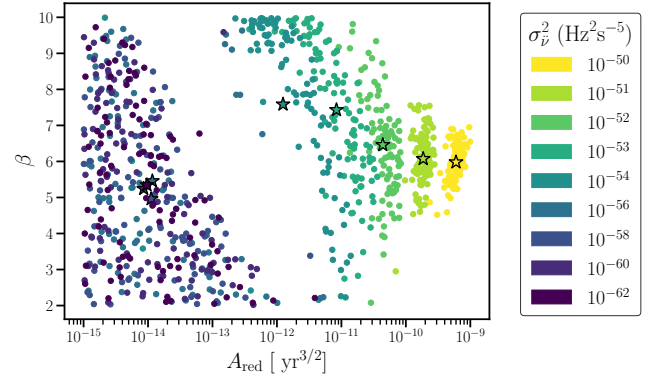


Figure 4. Relation between the injected Langevin noise amplitude squared, $\sigma_{\dot{\nu}}^2$ in (5) (units: $\text{Hz}^2 \text{ s}^{-5}$; see color scale) and the phase residual PSD parameters A_{red} (units: $\text{yr}^{3/2}$) and β in (10) inferred by TEMPONEST. Each round dot corresponds to one of the 100 random realizations analyzed in Figure 3. Stars denote $\langle A_{\text{red}} \rangle$ and $\langle \beta \rangle$ for the ensemble of 100 realizations at each of the nine values $\sigma_{\dot{\nu}}^2 / (1 \text{ Hz}^2 \text{ s}^{-5}) = 10^{-50}, 10^{-51}, 10^{-52}, 10^{-53}, 10^{-54}, 10^{-56}, 10^{-58}, 10^{-60}$, and 10^{-62} (indicated by the color scheme in the legend).

et al. 2020)? Equation (13) suggests that the answer is yes, because DISP(n) — and hence the condition DISP(n) $\gg 1$ — is independent of $\nu(t_0)$ and $\dot{\nu}(t_0)$. We check whether this is true empirically in this section by running tests on synthetic data.

To conduct the tests, we perform the following numerical experiment. We draw a random $\nu(t_0)$ from a uniform distribution, in the arbitrary but representative range $0.3 \leq \nu(t_0) / (1 \text{ Hz}) \leq 7.5$. Holding $\dot{\nu}(t_0)$ and n_{pl} fixed (i.e. using the injected values found in Table 2) we calculate $\dot{\nu}(t_0)$ via (1). We create a synthetic data realization, at a given $\sigma_{\dot{\nu}}^2$, for the random $\nu(t_0)$ and $\dot{\nu}(t_0)$ pair and feed it to TEMPONEST as detailed in Section 2.4. This process is repeated 100 times per $\sigma_{\dot{\nu}}^2$ value, with the latter variable covering $10^{-56} \leq \sigma_{\dot{\nu}}^2 / (1 \text{ Hz}^2 \text{ s}^{-5}) \leq 10^{-50}$ in steps of two decades. We calculate DISP(n) using (12). Hereafter we use the subscript “v”, viz. DISP_v(n), to label the previous procedure, i.e. varying $\nu(t_0)$ and $\dot{\nu}(t_0)$, as opposed to DISP(n) for the unique values of $\nu(t_0)$ and $\dot{\nu}(t_0)$ listed in Table 2 and presented in Section 4.1.

The results of the experiment are summarized in Table 4. DISP_v(n) (central column in Table 4) is presented alongside the fraction DISP_v(n)/DISP(n) (rightmost column in Table 4). The fraction DISP_v(n)/DISP(n) varies from 0.8 to 1.8 across six decades of $\sigma_{\dot{\nu}}^2$ values. In other words, DISP(n) depends weakly on $\nu(t_0)$ and $\dot{\nu}(t_0)$ in the regime of astrophysical interest. Furthermore, DISP_v(n) approximates DISP(n) more closely, as $\sigma_{\dot{\nu}}^2$ increases, and the measured n grows more anomalous. That is, we obtain DISP_v(n) \approx DISP(n) independent of $\nu(t_0)$ and $\dot{\nu}(t_0)$ in the regime where it matters most. It is not surprising that DISP_v(n)/DISP(n) deviates weakly from unity for lower $\sigma_{\dot{\nu}}^2$; the latter regime corresponds to region (i) in Figure 3, which does not obey the trend in (13). Again, however, one obtains $n \approx n_{\text{pl}}$ in region (i), so the braking index is not anomalous, and DISP(n) is less consequential.

One drawback of (13) when applied to real astronomical data is that the right-hand side involves $\dot{\nu}_{\text{em}}(t_0)$, which is difficult to measure accurately when timing noise masks the secular spin down — the central point, indeed, of this paper. Of course, one can obtain a fair estimate by assuming $\dot{\nu}_{\text{em}}(t_0) = n_{\text{pl}} \dot{\nu}(t_0)^2 / \nu(t_0) \sim \dot{\nu}(t_0)^2 / \nu(t_0)$

Table 4. Results of varying $\nu(t_0)$ and $\dot{\nu}(t_0)$ on the dispersion of n measurements. From left to right, the columns list the injected $\sigma_{\dot{\nu}}^2$, the dispersion when varying $\nu(t_0)$ and $\dot{\nu}(t_0)$, denoted $\text{DISP}_{\dot{\nu}}(n)$, and the fraction $\text{DISP}_{\dot{\nu}}(n)/\text{DISP}(n)$, with $\text{DISP}(n)$ copied from Figure 3.

$\sigma_{\dot{\nu}}^2 / \text{Hz}^2 \text{s}^{-5}$	$\text{DISP}_{\dot{\nu}}(n)$	$\text{DISP}_{\dot{\nu}}(n)/\text{DISP}(n)$
10^{-50}	3.6×10^6	1.0
10^{-52}	3.0×10^4	0.8
10^{-54}	4.9×10^2	1.4
10^{-56}	9.4×10^0	1.8

for most plausible physical torques (see Section 1), as suggested in Section 4.1. There is a second valid approach, however. Instead of the fractional variance $\text{DISP}(n)$, one can consider the absolute variance

$$\langle n^2 \rangle - n_{\text{pl}}^2 = \frac{\sigma_{\dot{\nu}}^2 v_{\text{em}}(t_0)^2}{\gamma_{\dot{\nu}}^2 \dot{v}_{\text{em}}(t_0)^4 T_{\text{obs}}} \quad (14)$$

Equation (14) does introduce new dependences on $v_{\text{em}}(t_0)$ and $\dot{v}_{\text{em}}(t_0)$, but the dependences are straightforward, and $v_{\text{em}}(t_0)$ and $\dot{v}_{\text{em}}(t_0)$ are always measured accurately in any pulsar for astrophysically plausible $\sigma_{\dot{\nu}}$ values, unlike $\dot{v}_{\text{em}}(t_0)$. The reader is encouraged to select between (13) or (14) to suit the application at hand.

5 CONCLUSIONS

Stochastic spin wandering (i.e. the achromatic component of timing noise unrelated to magnetospheric and interstellar propagation) introduces random dispersion into measurements of the braking index of a rotation-powered pulsar, masking the underlying, secular (e.g. electromagnetic) braking torque. We quantify the masking phenomenon in this paper through a combination of analytic theory and controlled, systematic, numerical experiments based on synthetic data and the pulsar timing software TEMPONEST. The synthetic data are generated for the representative model $\ddot{v}(t) = \dot{v}_{\text{em}}(t) + \zeta(t)$, where $v_{\text{em}}(t)$ satisfies $\dot{v}_{\text{em}}(t) = K v_{\text{em}}(t)^{n_{\text{pl}}}$ with $n_{\text{pl}} = 3$ and $K = \text{constant}$ in this paper for the sake of definiteness, and $\zeta(t)$ is a fluctuating, zero-mean, Langevin driver. Alternative models (e.g. with K varying) are equally valid and can be studied within the same framework. The synthetic TOAs are fed into TEMPO2 and TEMPONEST to produce two traditional timing solutions as a cross-check. TEMPONEST output is converted into a measurement of n for each random realization of the noise and compared with the injected value of n_{pl} .

The probability distribution of the synthetic n measurements, presented in Section 3 and Figure 2, reveals two important properties. First, the dispersion of n [as measured by $\text{DISP}(n)$, for example] for an ensemble of random noise realizations with fixed amplitude $\sigma_{\dot{\nu}}$ is typically greater than the formal uncertainty Δn returned by TEMPONEST for a single random noise realization with the same $\sigma_{\dot{\nu}}$ in the astrophysically relevant regime $\sigma_{\dot{\nu}}^2 \gtrsim 10^{-56} \text{Hz}^2 \text{s}^{-5}$. That is, the blue and cyan histograms in Figure 2 are wider than the orange histograms. Second, the dispersion of n is typically greater than n_{pl} in the same regime. That is, n_{pl} falls outside the range $[n - \Delta n, n + \Delta n]$ for more realizations, as $\sigma_{\dot{\nu}}^2 \gtrsim 10^{-56} \text{Hz}^2 \text{s}^{-5}$ increases. For example, at least 90% of the $[n - \Delta n, n + \Delta n]$ intervals include n_{pl} for $\sigma_{\dot{\nu}}^2 \leq 10^{-58} \text{Hz}^2 \text{s}^{-5}$. Yet, this percentage drops to 50% for $\sigma_{\dot{\nu}}^2 = 10^{-56} \text{Hz}^2 \text{s}^{-5}$ and 8% for $\sigma_{\dot{\nu}}^2 = 10^{-50} \text{Hz}^2 \text{s}^{-5}$. As an

astronomical observation of a real pulsar involves analyzing a single noise realization (the real one), and there is no way to know where that realization lies within the ensemble, the practical uncertainty in measuring n_{pl} (as opposed to n) for a real pulsar is governed by $\text{DISP}(n) \gg \Delta n$ rather than Δn .

The scaling of $\text{DISP}(n)$ versus $\sigma_{\dot{\nu}}$ in (13), derived analytically in Appendix A and confirmed by Monte Carlo simulations with synthetic data, is the central result of the paper. It applies in the high-noise regime $10^{-58} \leq \sigma_{\dot{\nu}}^2 / (1 \text{Hz}^2 \text{s}^{-5}) \leq 10^{-50}$, where anomalous braking indices $|n| \gg n_{\text{pl}}$ are measured. In the low-noise regime $\sigma_{\dot{\nu}}^2 \leq 10^{-58} \text{Hz}^2 \text{s}^{-5}$, one obtains $\text{DISP}(n) \lesssim 1$, and measurements return $n \approx n_{\text{pl}}$ instead. Reexpressing (13) equivalently as (14), one arrives at the condition

$$\sigma_{\dot{\nu}}^2 \gg 10^{-60} (\gamma_{\dot{\nu}} / 10^{-6} \text{s}^{-1})^2 (\dot{v} / 10^{-14} \text{Hz s}^{-1})^4 (\nu / 1 \text{Hz})^{-2} \times (T_{\text{obs}} / 10^8 \text{s}) \text{Hz}^2 \text{s}^{-5} \quad (15)$$

for the measured braking index $|n| \gg n_{\text{pl}}$ to be anomalous, such that n_{pl} is likely to fall outside the measured range $[n - \Delta n, n + \Delta n]$. Equation (15) may prove helpful in analyzing and interpreting real data in the future, because it is composed of observables: $\sigma_{\dot{\nu}}^2$ can be related to the PSD of the red noise phase residuals inferred by TEMPONEST, as discussed in Section 4.2 and Figure 4, and $\gamma_{\dot{\nu}}$ can be estimated approximately for the pulsar population as a whole from glitch recoveries or auto-correlation statistics, as discussed in Section 4.1.

One may wonder whether the dispersion in n measurements studied in this paper arises from the particular Brownian form of the timing noise dynamics postulated in Section 2.1, encapsulated by equations (2)–(9). The answer is no. The exact amount of dispersion does depend on the particular noise dynamics, as does the exact analytic form of the testable formula for $\text{DISP}(n)$ given by (13) or equivalently (14). However, the fact that the dispersion exists at all, and that the resulting braking indices are anomalous with $|n| \gg n_{\text{pl}}$, are generic features of any reasonable noise process of sufficient amplitude, not just the one in Section 2.1. We verify this by repeating the numerical experiments in Sections 2–4 for synthetic data generated according to the default noise process offered in TEMPO2, whose PSD is a power law defined by an amplitude and an exponent according to (10). The results are presented in Appendix B. We find that they are broadly the same as in Sections 2–4, e.g. the blue and cyan histograms in Figure 2 are unchanged qualitatively, and one still measures $|n| \gg n_{\text{pl}}$ under a range of circumstances. $\text{DISP}(n)$ for the power-law PSD in TEMPO2 is ~ 20 times smaller than predicted by (13) or (14).

Ultimately the ideas in this paper should be tested with real data. This brings some challenges. The tests in Sections 3 and 4, which examine under what conditions TEMPONEST recovers the “true”, underlying, secular n_{pl} , can be performed with synthetic data only, where the injected n_{pl} is known. In real data, n_{pl} is never known independently; no quantitative, predictive, electrodynamic theory of pulsar braking exists at present (Melrose & Yuen 2016). Nevertheless it may be possible, with sufficient data, to perform Bayesian model selection on a range of torque models in an effort to determine which one is preferred statistically. To do this, it is advantageous to convert the torque model (including stochastic spin wandering) into its state-space representation, so that a direct comparison can be made between the observed time series (e.g. TOAs) and the predictions of the model. Some promising steps have been made recently in this direction, for example when searching for pulsar glitches with a hidden Markov

model (Melatos et al. 2020; Dunn et al. 2022), or when estimating the parameters of the two-component, crust-superfluid model of a neutron star by coupling a Kalman filter to expectation-maximization or Markov chain Monte Carlo algorithms (Meyers et al. 2021b,a). It is a priority to apply the latter techniques, and others under development, to the high-quality data sets being generated by the latest generation of high-cadence pulsar timing campaigns (Namkham et al. 2019b,a; Lower et al. 2020; Parthasarathy et al. 2021; Johnston et al. 2021).

ACKNOWLEDGEMENTS

The authors thank Patrick Meyers, for discussing the Brownian model and making the baboo package freely available, and Liam Dunn, for guidance in the use of the TEMPONEST and TEMPO2 software infrastructure and advice that allowed the Brownian model to qualitatively emulate the phase residuals of PSR J0942–5552 in Figure 1. Additionally, we thank Patrick Meyers, Liam Dunn, Nicholas O’Neill, and Joe O’Leary for useful discussions regarding Section 4, which led ultimately to an understanding of local and nonlocal n measurements. We thank the anonymous referee for helpful suggestions which improved the manuscript. This research was supported by the Australian Research Council Centre of Excellence for Gravitational Wave Discovery (OzGrav), grant number CE170100004. A. F. Vargas is supported by a Melbourne Research Scholarship and by the N. D. Goldsworthy Scholarship for Physics. The numerical calculations were performed on the OzSTAR supercomputer facility at Swinburne University of Technology. The OzSTAR program receives funding in part from the Astronomy National Collaborative Research Infrastructure Strategy (NCRIS) allocation provided by the Australian Government.

DATA AVAILABILITY

The timing solution for PSR J0942–5552 comes from Lower et al. (2020). All the synthetic data are generated using the open access software package baboo available at <http://www.github.com/meyers-academic/baboo> (Meyers et al. 2021b). We use TEMPO2 (Hobbs et al. 2006) and TEMPONEST (Lentati et al. 2014) to obtain timing solutions for the synthetic data.

REFERENCES

- Akbal O., Alpar M. A., Buchner S., Pines D., 2017, *Monthly Notices of the Royal Astronomical Society*, 469, 4183
- Akbal O., Güğercinoğlu E., Alpar M. A., 2021, arXiv e-prints, p. arXiv:2106.03341
- Alpar M. A., Baykal A., 2006, *MNRAS*, 372, 489
- Alpar M. A., Nandkumar R., Pines D., 1986, *ApJ*, 311, 197
- Andersson N., 1998, *ApJ*, 502, 708
- Antonelli M., Basu A., Haskell B., 2022, arXiv e-prints, p. arXiv:2206.10416
- Archibald R. F., et al., 2016, *ApJ*, 819, L16
- Arons J., 1992, in Hanks T. H., Rankin J. M., Gil J. A., eds, IAU Colloq. 128: Magnetospheric Structure and Emission Mechanics of Radio Pulsars. p. 56
- Arzoumanian Z., Nice D. J., Taylor J. H., Thorsett S. E., 1994, *ApJ*, 422, 671
- Barsukov D. P., Tsygan A. I., 2010, *MNRAS*, 409, 1077
- Barsukov D. P., Polyakova P. I., Tsygan A. I., 2009, *Astronomy Reports*, 53, 1146
- Biryukov A., Beskin G., Karpov S., 2012, *MNRAS*, 420, 103
- Blandford R. D., Romani R. W., 1988, *MNRAS*, 234, 57P
- Bucciantini N., Thompson T. A., Arons J., Quataert E., Del Zanna L., 2006, *MNRAS*, 368, 1717
- Cheng K. S., 1987, *ApJ*, 321, 799
- Chukwude A. E., 2003, *A&A*, 406, 667
- Chukwude A. E., Chidi Odo F., 2016, *Research in Astronomy and Astrophysics*, 16, 150
- Chukwude A. E., Baiden A. A., Onuchukwu C. C., 2010, *A&A*, 515, A21
- Coles W., Hobbs G., Champion D. J., Manchester R. N., Verbiest J. P. W., 2011, *MNRAS*, 418, 561
- Contopoulos I., Spitkovsky A., 2006, *ApJ*, 643, 1139
- Cordes J. M., 1980, *ApJ*, 237, 216
- Cordes J. M., Downs G. S., 1985, *ApJS*, 59, 343
- Cordes J. M., Helfand D. J., 1980, *ApJ*, 239, 640
- D’Alessandro F., McCulloch P. M., Hamilton P. A., Deshpande A. A., 1995, *MNRAS*, 277, 1033
- Dunn L., et al., 2022, *MNRAS*, 512, 1469
- Fuentes J. R., Espinoza C. M., Reisenegger A., Shaw B., Stappers B. W., Lyne A. G., 2017, *A&A*, 608, A131
- Gardiner C. W., 1994, *Handbook of stochastic methods for physics, chemistry and the natural sciences*
- Geppert U., Rheinhardt M., 2002, *A&A*, 392, 1015
- Goglichidze O. A., Barsukov D. P., Tsygan A. I., 2015, *MNRAS*, 451, 2564
- Goldreich P., 1970, *ApJ*, 160, L11
- Goncharov B., et al., 2021, *MNRAS*, 502, 478
- Gourgouliatos K. N., Cumming A., 2015, *MNRAS*, 446, 1121
- Güğercinoğlu E., 2017, *MNRAS*, 469, 2313
- Güğercinoğlu E., Alpar M. A., 2014, *ApJ*, 788, L11
- Gunn J. E., Ostriker J. P., 1969, *Nature*, 221, 454
- Hobbs G. B., Edwards R. T., Manchester R. N., 2006, *MNRAS*, 369, 655
- Johnston S., Galloway D., 1999, *MNRAS*, 306, L50
- Johnston S., Karastergiou A., 2017, *MNRAS*, 467, 3493
- Johnston S., et al., 2021, *MNRAS*, 502, 1253
- Jones P. B., 1990, *MNRAS*, 246, 364
- Kou F. F., Tong H., 2015, *MNRAS*, 450, 1990
- Lentati L., Alexander P., Hobson M. P., Feroz F., van Haasteren R., Lee K. J., Shannon R. M., 2014, *MNRAS*, 437, 3004
- Lentati L., et al., 2016, *MNRAS*, 458, 2161
- Link B., Epstein R. I., 1997, *ApJ*, 478, L91
- Livingstone M. A., Kaspi V. M., 2011, *ApJ*, 742, 31
- Livingstone M. A., Kaspi V. M., Gavriil F. P., Manchester R. N., Gotthelf E. V. G., Kuiper L., 2007, *Ap&SS*, 308, 317
- Lower M. E., et al., 2020, *MNRAS*, 494, 228
- Lower M. E., et al., 2021, *MNRAS*, 508, 3251
- Lyne A. G., Pritchard R. S., Graham Smith F., 1993, *Monthly Notices of the Royal Astronomical Society*, 265, 1003
- Lyne A. G., Pritchard R. S., Graham-Smith F., Camilo F., 1996, *Nature*, 381, 497
- Manchester R. N., Hobbs G. B., Teoh A., Hobbs M., 2005, *AJ*, 129, 1993
- Melatos A., 1997, *MNRAS*, 288, 1049
- Melatos A., 2000, *MNRAS*, 313, 217
- Melatos A., Link B., 2014, *MNRAS*, 437, 21
- Melatos A., Dunn L. M., Suvorova S., Moran W., Evans R. J., 2020, *ApJ*, 896, 78
- Melrose D. B., Yuen R., 2016, *Journal of Plasma Physics*, 82, 635820202
- Meyers P. M., Melatos A., O’Neill N. J., 2021a, *MNRAS*, 502, 3113
- Meyers P. M., O’Neill N. J., Melatos A., Evans R. J., 2021b, *MNRAS*, 506, 3349
- Michel F. C., Tucker W. H., 1969, *Nature*, 223, 277
- Namkham N., Jaroenjittichai P., Johnston S., 2019a, *MNRAS*, 487, 5854
- Namkham N., Jaroenjittichai P., Johnston S., 2019b, in *Journal of Physics Conference Series*. p. 012161, doi:10.1088/1742-6596/1380/1/012161
- Owen B. J., Lindblom L., Cutler C., Schutz B. F., Vecchio A., Andersson N., 1998, *Phys. Rev. D*, 58, 084020
- Papaloizou J., Pringle J. E., 1978, *MNRAS*, 182, 423
- Parthasarathy A., et al., 2019, *MNRAS*, 489, 3810
- Parthasarathy A., et al., 2020, *MNRAS*, 494, 2012
- Parthasarathy A., et al., 2021, *MNRAS*, 502, 407
- Pétri J., 2015, *MNRAS*, 450, 714
- Pétri J., 2016, *MNRAS*, 463, 1240
- Pétri J., 2017, *MNRAS*, 472, 3304
- Pons J. A., Viganò D., Geppert U., 2012, *A&A*, 547, A9
- Price S., Link B., Shore S. N., Nice D. J., 2012, *MNRAS*, 426, 2507
- Rößler A., 2010, *SIAM Journal on Numerical Analysis*, 48, 922
- Shannon R. M., Cordes J. M., 2010, *ApJ*, 725, 1607
- Tauris T. M., Konar S., 2001, *A&A*, 376, 543
- Thorne K. S., 1980, *Reviews of Modern Physics*, 52, 299
- Urama J. O., Link B., Weisberg J. M., 2006, *MNRAS*, 370, L76
- Wasserman I., Cordes J. M., Chatterjee S., Batra G., 2022, *ApJ*, 928, 53
- Zhang C.-M., et al., 2022, *Universe*, 8, 628

APPENDIX A: THEORY OF ANOMALOUS BRAKING INDICES

In this appendix, we present an analytic theory of anomalous braking indices, which relates the statistics of the measured n value to its secular component n_{pl} and to the properties of the stochastic spin wandering, including importantly the amplitude $\sigma_{\dot{\nu}}$. The central result is a prediction for the dispersion $\text{DISP}(n)$ as a function of $\sigma_{\dot{\nu}}$ [see equation (13)] and hence a condition on $\sigma_{\dot{\nu}}$ which, when satisfied, implies $|n| \gg n_{\text{pl}}$. To this end, we present in Appendix A1 the analytical solution for the Brownian model described by the system of stochastic differential equations (2)–(9). We use the analytic solution of (2)–(9) to calculate the statistics of n , when n is measured in two ways: “nonlocally”, via a finite difference formula involving $\dot{\nu}(t_0)$ and $\dot{\nu}(t_0 + T_{\text{obs}})$, and “locally”, by calculating the second derivative $\ddot{\nu}$ directly from the component $X_4(t)$ of the state vector in (2). The nonlocal and local approaches are described and justified in Appendices A2 and A3 respectively.

A1 Analytic solution of the Brownian model (2)–(9)

In preparation for solving (2)–(9), we write out the right-hand side of (2) in the familiar Langevin form

$$\frac{d\phi(t)}{dt} = \nu(t), \quad (\text{A1})$$

$$\frac{d\nu(t)}{dt} = -\gamma_\nu[\nu(t) - \nu_{\text{em}}(t)] + \dot{\nu}(t), \quad (\text{A2})$$

$$\frac{d\dot{\nu}(t)}{dt} = -\gamma_{\dot{\nu}}[\dot{\nu}(t) - \dot{\nu}_{\text{em}}(t)] + \ddot{\nu}(t), \quad (\text{A3})$$

$$\frac{d\ddot{\nu}(t)}{dt} = -\gamma_{\ddot{\nu}}[\ddot{\nu}(t) - \ddot{\nu}_{\text{em}}(t)] + \ddot{\xi}(t), \quad (\text{A4})$$

where $\xi(t)$ is a white noise driver, with $\langle \xi(t) \rangle = 0$ and $\langle \xi(t)\xi(t') \rangle = \sigma_\xi^2 \delta(t - t')$. In (A2)–(A4), the secular braking behavior takes the form

$$\nu_{\text{em}}(t) = \nu_{\text{em}}(t_0) \left(1 + \frac{t}{\tau}\right)^{-(n_{\text{pl}}-1)^{-1}}, \quad (\text{A5})$$

where

$$\tau = -\frac{\nu_{\text{em}}(t_0)}{(n_{\text{pl}} - 1)\dot{\nu}_{\text{em}}(t_0)}, \quad (\text{A6})$$

is the characteristic spin-down age, and $\dot{\nu}_{\text{em}}(t)$, $\ddot{\nu}_{\text{em}}(t)$, and $\ddot{\xi}(t)$ are the first, second, and third derivatives of (A5), respectively.

Equations (A2)–(A4) are solvable by means of an integrating factor. Setting $\nu(t_0) = \nu_{\text{em}}(t_0)$, $\dot{\nu}(t_0) = \dot{\nu}_{\text{em}}(t_0)$, $\ddot{\nu}(t_0) = \ddot{\nu}_{\text{em}}(t_0)$, and $t_0 = 0$ without loss of generality, we obtain

$$\nu(t) = \nu_{\text{em}}(t) + e^{-\gamma_\nu t} \int_0^t dt' e^{\gamma_\nu t'} [\dot{\nu}(t') - \dot{\nu}_{\text{em}}(t')], \quad (\text{A7})$$

$$\dot{\nu}(t) = \dot{\nu}_{\text{em}}(t) + e^{-\gamma_{\dot{\nu}} t} \int_0^t dt' e^{\gamma_{\dot{\nu}} t'} [\ddot{\nu}(t') - \ddot{\nu}_{\text{em}}(t')], \quad (\text{A8})$$

$$\ddot{\nu}(t) = \ddot{\nu}_{\text{em}}(t) + e^{-\gamma_{\ddot{\nu}} t} \int_0^t dt' e^{\gamma_{\ddot{\nu}} t'} \ddot{\xi}(t'). \quad (\text{A9})$$

We then integrate (A1) directly to obtain

$$\phi(t) = \phi(0) + \int_0^t dt' \nu(t'). \quad (\text{A10})$$

The initial phase is a historical accident, so we take $\phi(0) = 0$ without loss of generality.

It is straightforward to calculate the covariances of the zero-mean fluctuating variables $\delta\nu(t) = \nu(t) - \nu_{\text{em}}(t)$, $\delta\dot{\nu}(t) = \dot{\nu}(t) - \dot{\nu}_{\text{em}}(t)$, and $\delta\ddot{\nu}(t) = \ddot{\nu}(t) - \ddot{\nu}_{\text{em}}(t)$ starting from (A7)–(A9). For example (A9) implies

$$\langle \delta\ddot{\nu}(t)\delta\ddot{\nu}(t') \rangle = e^{-2\gamma_{\ddot{\nu}} t} \int_0^t dt' e^{\gamma_{\ddot{\nu}} t'} \int_0^{t'} dt'' e^{\gamma_{\ddot{\nu}} t''} \langle \xi(t')\xi(t'') \rangle, \quad (\text{A11})$$

$$= \frac{\sigma_\xi^2}{2\gamma_{\ddot{\nu}}} \left(1 - e^{-2\gamma_{\ddot{\nu}} t}\right). \quad (\text{A12})$$

We combine (A12) with (A8) and (A9) to obtain

$$\begin{aligned} \langle \delta\dot{\nu}(t)^2 \rangle &= \frac{\sigma_\xi^2}{2\gamma_{\ddot{\nu}}\gamma_{\dot{\nu}}(\gamma_{\ddot{\nu}} - \gamma_{\dot{\nu}})^2(\gamma_{\dot{\nu}} + \gamma_{\ddot{\nu}})} \\ &\times \left[(\gamma_{\dot{\nu}} - \gamma_{\ddot{\nu}})^2 + 4\gamma_{\dot{\nu}}\gamma_{\ddot{\nu}}e^{-(\gamma_{\dot{\nu}} + \gamma_{\ddot{\nu}})t} \right. \\ &\left. - (\gamma_{\dot{\nu}} + \gamma_{\ddot{\nu}}) \left(\gamma_{\ddot{\nu}}e^{-2\gamma_{\dot{\nu}}t} + \gamma_{\dot{\nu}}e^{-2\gamma_{\ddot{\nu}}t} \right) \right] \end{aligned} \quad (\text{A13})$$

and

$$\begin{aligned} \langle \delta\dot{\nu}(t)\delta\ddot{\nu}(t) \rangle &= \frac{\sigma_\xi^2}{\gamma_{\ddot{\nu}}(\gamma_{\dot{\nu}}^2 - \gamma_{\ddot{\nu}}^2)} \left[-\gamma_{\ddot{\nu}}e^{-(\gamma_{\dot{\nu}} + \gamma_{\ddot{\nu}})t} \right. \\ &\left. + \frac{\gamma_{\dot{\nu}}}{2} \left(1 + e^{-2\gamma_{\dot{\nu}}t}\right) - \frac{\gamma_{\ddot{\nu}}}{2} \left(1 - e^{-2\gamma_{\ddot{\nu}}t}\right) \right]. \end{aligned} \quad (\text{A14})$$

Equations (A12)–(A14) hold regardless of the form of $\nu_{\text{em}}(t)$. In other words, when deriving (A12)–(A14), we do not need to make the approximation $t \leq T_{\text{obs}} \ll \tau$.

The above analytic solution reproduces qualitatively the observed timing behavior of typical pulsars in the ATNF Pulsar Database (Manchester et al. 2005), as illustrated in Figure 1 for the representative object PSR J0942–5552. Specifically, the analytic solution has the following properties.

(i) It exhibits fluctuations in $\nu(t)$, $\dot{\nu}(t)$ and $\ddot{\nu}(t)$ driven by $\xi(t)$ in (A4). The fluctuation amplitude matches the observed timing behavior of typical pulsars (e.g. Figure 1 and Table 2) in the following, well-defined regime: $\gamma_\nu \sim \gamma_{\dot{\nu}} \ll T_{\text{obs}}^{-1} \ll \gamma_{\ddot{\nu}}$. When the foregoing conditions hold simultaneously, one obtains $|\delta\nu(t)| \ll \nu_{\text{em}}(t)$, $|\delta\dot{\nu}(t)| \ll |\dot{\nu}_{\text{em}}(t)|$, and $|\delta\ddot{\nu}(t)| \gg |\ddot{\nu}_{\text{em}}(t)|$, as observed typically (Lower et al. 2020; Parthasarathy et al. 2020). Incidentally, the foregoing conditions are also consistent with theoretical predictions of γ_ν , $\gamma_{\dot{\nu}}$, and $\gamma_{\ddot{\nu}}$ based on pulsar glitch recoveries and timing noise auto-correlation studies (Price et al. 2012; Melatos et al. 2020; Meyers et al. 2021a,b). In the above regime, for $t \leq T_{\text{obs}}$, we approximate (A12)–(A14) as

$$\langle \delta\ddot{\nu}(t)^2 \rangle = \frac{\sigma_\xi^2}{2\gamma_{\ddot{\nu}}} \quad (\text{A15})$$

$$\langle \delta\dot{\nu}(t)^2 \rangle = \frac{\sigma_\xi^2}{2\gamma_{\dot{\nu}}\gamma_{\ddot{\nu}}} \left(1 - e^{-2\gamma_{\dot{\nu}}t}\right), \quad (\text{A16})$$

and

$$\langle \delta\dot{\nu}(t)\delta\ddot{\nu}(t) \rangle = \frac{\sigma_\xi^2}{2\gamma_{\ddot{\nu}}}. \quad (\text{A17})$$

(ii) The variances $\langle \delta\dot{\nu}(t)^2 \rangle$ and $\langle \delta\ddot{\nu}(t)^2 \rangle$ are bounded and small in the sense defined in (i), ensuring that pulsars do not reverse the sign of their spin or torque after birth. Moreover, the covariance $\langle \delta\dot{\nu}(t)\delta\ddot{\nu}(t') \rangle$ behaves well for all t and t' , does not diverge in the limit $t \rightarrow t'$, and stays bounded as $t = t' \leq T_{\text{obs}}$ increases. This is important, because measuring n involves measuring $\ddot{\nu}(t)$; that is, $\nu(t)$ must be differentiable twice in order to produce a well-behaved observable. In contrast, the third derivative $\ddot{\nu}(t) \propto \xi(t)$ is not differentiable, and the covariance $\langle \ddot{\nu}(t)\ddot{\nu}(t') \rangle \propto \delta(t - t')$ diverges for $t \rightarrow t'$, as expected for the highest-order derivatives in any Brownian model, but these behaviors do not affect the observable n ; see also footnote 2.

(iii) $\langle \dot{v}(t) \rangle$ and $\langle \ddot{v}(t) \rangle$ have sensible long-term values consistent with $n = n_{\text{pl}}$. The ensemble average of (A8) yields $\langle \dot{v}(t) \rangle = \dot{v}_{\text{em}}(t)$. Likewise the ensemble average of (A9) yields $\langle \ddot{v}(t) \rangle = \ddot{v}_{\text{em}}(t)$.

A2 Nonlocal measurement of n

In a deterministic system, where $\dot{v}(t)$ is a smooth function, $\ddot{v}(t)$ is approximated accurately by $\ddot{v}(t) \approx [\dot{v}(t + \Delta t) - \dot{v}(t)]/\Delta t$, provided that Δt is small. In the stochastic system (2)–(9), $\ddot{v}(t)$ fluctuates randomly on arbitrary short timescales, and the approximation $\ddot{v}(t) \approx [\dot{v}(t + \Delta t) - \dot{v}(t)]/\Delta t$ breaks down even for small Δt . Fundamentally, this discrepancy is caused by $\xi(t)$ in (A9) being nondifferentiable, as discussed in Appendix A1 and footnote 2. In general, although $X_4(t) = \ddot{v}(t)$ in (2) exists instantaneously, there is no unique way of estimating $\ddot{v}(t)$ from measured values of $\dot{v}(t)$; the results for $\ddot{v}(t)$ and hence n depends on exactly how the measurement is made.

In this section, we formulate a nonlocal measurement of n , in which $\ddot{v}(t)$ is evaluated by finite differencing the time series $\dot{v}(t)$ at two distinct times t_1 and $t_2 > t_1$, which are not separated infinitesimally; indeed, the usual choice in practice is $t_2 = t_1 + T_{\text{obs}}$. The nonlocal approach is consistent with standard approaches to measuring n using TEMPONEST for real pulsars (Lower et al. 2020; Parthasarathy et al. 2020). Following equation (6) in Johnston & Galloway (1999), we calculate n from

$$n = 1 - \frac{\dot{v}(t_1)v(t_2) - \dot{v}(t_2)v(t_1)}{\dot{v}(t_1)\dot{v}(t_2)T_{\text{obs}}}, \quad (\text{A18})$$

where $v(t_1)$, $\dot{v}(t_1)$, $v(t_2)$, and $\dot{v}(t_2)$ are measurements done at times t_1 and $t_2 = t_1 + T_{\text{obs}}$. Equation (A18) is obtained by integrating $\dot{v}(t) = -Kv(t)^n$ from $t = t_1$ to $t = t_2$ and eliminating K via $K = -\dot{v}(t_1)/v(t_1)^n$.

Consider the regime $\gamma_v \sim \gamma_{\dot{v}} \ll T_{\text{obs}}^{-1} \ll \gamma_{\ddot{v}}$ identified in point (i) of Appendix A1, which guarantees that $\delta v(t)$ and $\delta \dot{v}(t)$ are fluctuating terms with zero mean which obey $|\delta v(t)| \ll |v_{\text{em}}(t)|$ and $|\delta \dot{v}(t)| \ll |\dot{v}_{\text{em}}(t)|$. For example, we find $\delta v(t) \sim 10^{-8}|v_{\text{em}}(t)|$ and $\delta \dot{v} \sim 10^{-3}|\dot{v}_{\text{em}}(t)|$ for PSR J0942–5552 in Figure 1. In this regime, we can write,

$$\frac{v(t_2)}{\dot{v}(t_2)} = \frac{v_{\text{em}}(t_2) + \delta v(t_2)}{\dot{v}_{\text{em}}(t_2) [1 + \delta \dot{v}(t_2)/\dot{v}_{\text{em}}(t_2)]}, \quad (\text{A19})$$

$$\approx \frac{v_{\text{em}}(t_2)}{\dot{v}_{\text{em}}(t_2)} \left[1 + \frac{\delta v(t_2)}{v_{\text{em}}(t_2)} - \frac{\delta \dot{v}(t_2)}{\dot{v}_{\text{em}}(t_2)} \right], \quad (\text{A20})$$

and similarly for $v(t_1)/\dot{v}(t_1)$. Upon substituting (A20) into (A18), we obtain

$$n = 1 - \frac{1}{T_{\text{obs}}} \frac{v_{\text{em}}(t_2)}{\dot{v}_{\text{em}}(t_2)} \left[1 + \frac{\delta v(t_2)}{v_{\text{em}}(t_2)} - \frac{\delta \dot{v}(t_2)}{\dot{v}_{\text{em}}(t_2)} \right] + \frac{1}{T_{\text{obs}}} \frac{v_{\text{em}}(t_1)}{\dot{v}_{\text{em}}(t_1)} \left[1 + \frac{\delta v(t_1)}{v_{\text{em}}(t_1)} - \frac{\delta \dot{v}(t_1)}{\dot{v}_{\text{em}}(t_1)} \right]. \quad (\text{A21})$$

The ensemble average of (A21) yields

$$\langle n \rangle = 1 - \frac{1}{T_{\text{obs}}} \left[\frac{v_{\text{em}}(t_2)}{\dot{v}_{\text{em}}(t_2)} - \frac{v_{\text{em}}(t_1)}{\dot{v}_{\text{em}}(t_1)} \right] \quad (\text{A22})$$

$$= n_{\text{pl}}, \quad (\text{A23})$$

where the last line follows by comparing (A22) with (A18) for $\dot{v}_{\text{em}}(t) = -Kv_{\text{em}}^{n_{\text{pl}}}(t)$. We note further that $|\delta v(t)/v_{\text{em}}(t)| \ll |\delta \dot{v}(t)/\dot{v}_{\text{em}}(t)|$ holds empirically for all pulsars observed to date (Lower et al. 2020; Parthasarathy et al. 2020). Applying the latter inequality, and noting $v(t_1)/v(t_2) = 1 + \mathcal{O}(T_{\text{obs}}/\tau) \approx 1$, we combine (A21) and (A23) without the $\delta \dot{v}$ terms to obtain

$$n - n_{\text{pl}} \approx \frac{v_{\text{em}}(t_1)}{\dot{v}_{\text{em}}(t_1)^2} \left[\frac{\delta \dot{v}(t_2) - \delta \dot{v}(t_1)}{T_{\text{obs}}} \right]. \quad (\text{A24})$$

In effect, equation (A24) calculates n by replacing $\ddot{v}_{\text{em}}(t)$ with its first order (Euler) finite difference approximation. However, the approximation is not ad hoc; it follows from the empirically justified limits taken in the lead-up to (A24).

Ultimately we are interested in the fractional dispersion across the ensemble of noise realizations, i.e. equation (12). Therefore we need to calculate $\langle [\delta \dot{v}(t_2) - \delta \dot{v}(t_1)]^2 \rangle$. Setting $t = T_{\text{obs}}$ in (A16), with the time origin arbitrary (e.g. $t_1 = t_0$), we arrive at

$$\text{DISP}(n) = \frac{\sigma_{\dot{v}}^2(1 - e^{-2\gamma_{\dot{v}}T_{\text{obs}}})}{2\gamma_{\dot{v}}^2\gamma_v T_{\text{obs}}^2 \dot{v}_{\text{em}}^2(t_0)}. \quad (\text{A25})$$

In the astrophysically relevant regime $\gamma_v T_{\text{obs}} \ll 1$, (A25) reduces to

$$\text{DISP}(n) = \frac{\sigma_{\dot{v}}^2}{\gamma_{\dot{v}}^2 \dot{v}_{\text{em}}^2(t_0) T_{\text{obs}}}. \quad (\text{A26})$$

Equation (A26) is identical to (13).

A3 Local measurement of n

The nonlocal measurement of $\ddot{v}(t)$ and hence n in Appendix A2 is not unique. Valid alternative recipes exist, as foreshadowed above, which may or may not yield the same result as (A26) for $\text{DISP}(n)$. One alternative is a local measurement, in which n is obtained directly from the second-derivative component $X_4(t) = \ddot{v}(t)$ of the state vector in (2), as opposed to the finite difference approximation presented in Appendix A2.

To calculate $\text{DISP}(n)$ in this regime, we start from (1) and write

$$n(t)^2 = \frac{v_{\text{em}}^2(t) [\ddot{v}_{\text{em}}(t) + \delta \ddot{v}(t)]^2}{[\dot{v}_{\text{em}}(t) + \delta \dot{v}(t)]^4} \quad (\text{A27})$$

$$\approx n_{\text{pl}}^2 \left[1 + \frac{\delta \ddot{v}(t)}{\ddot{v}_{\text{em}}(t)} + \frac{\delta \dot{v}(t)^2}{\dot{v}_{\text{em}}(t)^2} \right] \left[1 - \frac{4\delta \dot{v}(t)}{\dot{v}_{\text{em}}(t)} + \frac{10\delta \dot{v}(t)^2}{\dot{v}_{\text{em}}(t)^2} \right] \quad (\text{A28})$$

locally, noting that one has $|\delta \dot{v}(t)| \ll |\dot{v}_{\text{em}}(t)|$ empirically for all observed pulsars. Taking the ensemble average of (A28), we obtain

$$\langle n(t)^2 \rangle = n_{\text{pl}}^2 \left[1 + \frac{10\langle \delta \dot{v}(t)^2 \rangle}{\dot{v}_{\text{em}}(t)^2} - \frac{8\langle \delta \ddot{v}(t)\delta \dot{v}(t) \rangle}{\dot{v}_{\text{em}}(t)\ddot{v}_{\text{em}}(t)} + \frac{\langle \delta \ddot{v}(t)^2 \rangle}{\ddot{v}_{\text{em}}(t)^2} \right]. \quad (\text{A29})$$

Equations (A15)–(A17) imply that the rightmost term in (A29) is

the biggest contributor in the astrophysically relevant regime $\gamma_{\dot{\nu}} \sim \gamma_{\dot{\nu}} \ll T_{\text{obs}}^{-1} \ll \gamma_{\dot{\nu}}$ considered in Appendix A1. Therefore to leading order (12) reduces to

$$\text{DISP}(n) = \frac{\sigma_{\dot{\nu}}^2}{2\gamma_{\dot{\nu}}\dot{\nu}_{\text{em}}^2(t_0)}. \quad (\text{A30})$$

Equation (A30) equals (A26) multiplied by the factor $\gamma_{\dot{\nu}}T_{\text{obs}}/2$.

One might ask: is (A26) the “true” $\text{DISP}(n)$, or is it (A30)? The answer is both. The local and nonlocal definitions represent two different “instruments” for measuring n . Both instruments measure $\langle n \rangle = n_{\text{pl}}$ correctly (without bias) upon performing an ensemble average. However, such an ensemble average cannot be done in practice when analyzing astronomical data, because one observes a single noise realization (the actual one) from a pulsar, and there is no way to know where it lies within the ensemble. On the other hand, the spread of n measurements with the nonlocal instrument is smaller by a factor $2(\gamma_{\dot{\nu}}T_{\text{obs}})^{-1}$ than with the local instrument. This is expected, because $\dot{\nu}$ fluctuates randomly on arbitrarily short time-scales according to the Brownian model (2)–(9), and a local (i.e. instantaneous) measurement of $\dot{\nu}$ inherits greater dispersion from these fluctuations than a nonlocal measurement, which effectively smooths $\dot{\nu}$ over T_{obs} .

APPENDIX B: $\text{DISP}(n)$ FOR SPIN WANDERING GENERATED WITH THE POWER-LAW RED-NOISE MODEL IN TEMPO2

The Brownian model defined by (2)–(9), known formally as an inhomogeneous Ornstein-Uhlenbeck process (Gardiner 1994), represents an idealized description of pulsar timing noise and is not unique. Other valid noise models exist, e.g. based on a Wiener process (Cordes 1980). It is therefore natural to ask whether or not the results in Sections 3 and 4 are general. The answer is yes: the formulas (13) and (14) for $\text{DISP}(n)$ as a function of $\sigma_{\dot{\nu}}$ are specific to the Brownian model in Section 2.1, but the existence of anomalous braking indices with $\langle n^2 \rangle^{1/2} \gg n_{\text{pl}}$ arising from dispersion among random noise realizations is a general property of any spin wandering process of sufficient amplitude. In this appendix, we demonstrate the point by repeating the analysis in Section 3 for synthetic data generated by the default red-noise PSD (10) offered within TEMPO2. Specifically, we confirm that: (i) we obtain $\text{DISP}(n) \gg 1$ for $6 \leq \beta \leq 8$ and $A_{\text{red}} \gtrsim 10^{-10} \text{ yr}^{3/2}$ sufficiently large; and (ii) we obtain $\text{DISP}(n) \gg 1$ even if we use (10) both to generate the synthetic data with TEMPO2 and measure n with TEMPONEST. That is, dispersion produces anomalous braking indices, whether the noise processes realized in the data and assumed in the analysis are the same or not, although $\text{DISP}(n)$ is greater in the latter scenario of course. The analysis in this appendix builds on similar tests in the literature, e.g. in Section 3 of Parthasarathy et al. (2020).

To perform the experiment, we generate 100 random realizations of synthetic data per value of A_{red} and β . We choose A_{red} and β to be consistent with the range of $\sigma_{\dot{\nu}}^2$ studied in Section 3 and Figure 4 to enable a fair comparison. Specifically, we choose $[A_{\text{red}}/(1 \text{ yr}^{3/2}), \beta] = (10^{-9.2}, 5.9), (10^{-9.7}, 6.1), (10^{-10.3}, 6.5), (10^{-11.1}, 7.4),$ and $(10^{-11.9}, 7.6)$, which correspond to $\sigma_{\dot{\nu}}^2/(1 \text{ Hz}^2 \text{ s}^{-5}) = 10^{-50}, 10^{-51}, 10^{-52}, 10^{-53},$ and 10^{-54} , respectively. In other words, the power-law PSD (10) is employed both when generating the noise in the synthetic data

(with TEMPO2) and when analysing the synthetic data to measure n (with TEMPONEST). The aforementioned values of A_{red} and β are consistent with recovered timing noise parameters in the pulsar population (Lower et al. 2020). All simulations use the rotational parameters displayed in Table 2. We set TEMPONEST priors as in Tables 1 and 3, except for $\dot{\nu}$ whose prior is set as detailed in Section 2.3.

Figure B1 summarizes the results of the above test in the same format as Figure 2. Each panel features three histograms: a blue one, which displays the distribution of measured $n > 0$ values, a cyan one, which displays the distribution of $n < 0$ values, and an orange one, which displays the distribution of formal uncertainties Δn reported by TEMPONEST via (11). The panels are arranged from top to bottom in order of decreasing A_{red} , which is analogous to decreasing $\sigma_{\dot{\nu}}$ (effective value) in Figure 2. The figure makes three key points. First, the blue and cyan histograms are wider than the orange histograms for $A_{\text{red}} \gtrsim 10^{-11.9} \text{ yr}^{3/2}$, as in Figure 2; that is, Δn is smaller than the dispersion arising from the ensemble of random realizations, even though the same timing noise model (10) is used to both generate and analyze the data. Second, anomalous braking indices with $|n| \gg n_{\text{pl}}$ are measured routinely for $A_{\text{red}} \gtrsim 10^{-9.2} \text{ yr}^{3/2}$, as in Figure 2, and n can take either sign, in line with the findings in Section 3 and observational studies (Johnston & Galloway 1999; Chukwude & Chidi Odo 2016; Parthasarathy et al. 2020; Lower et al. 2020). Third, $\text{DISP}(n)$ is systematically smaller by a factor of ~ 20 than in Figure 2, because the same timing noise model (10) is used to both generate and analyze the data.

Let us quantify briefly the three points above. The FWHMs of the summed blue and cyan histograms grow with the amplitude of the power-law timing noise. The FWHM rises from $11n_{\text{pl}}$ for the bottom panel to $823n_{\text{pl}}$ for the top panel. The percentage of recovered $n \pm \Delta n$ intervals that include n_{pl} is 55% and 57% for the bottom and the top panels, respectively. $\text{DISP}(n)$ also grows, from $\text{DISP}(n) = 35$ for the bottom panel to $\text{DISP}(n) = 1.3 \times 10^5$ for the top panel, as the histograms shift rightward along the logarithmic horizontal axis. The measured values of $\text{DISP}(n)$, going from the top to the bottom panel, are 28, 10, 23, 20, and 10 times smaller than those in Sections 3 and 4 for the corresponding $\sigma_{\dot{\nu}}^2$ value.

In this appendix, as in Sections 3 and 4, TEMPONEST overestimates $|\dot{\nu}|$ and underestimates $\Delta\dot{\nu}$ on average across the ensemble of trials. Consequently, even when the same model generates and analyzes the data, the measured braking index can be anomalous, with n_{pl} falling outside of the measured range $[n - \Delta n, n + \Delta n]$. However, the incidence of anomalous braking indices is higher (i.e. $\text{DISP}(n)$ is greater), when different models are used to generate and analyze the data, as in Sections 3 and 4.

This paper has been typeset from a \LaTeX file prepared by the author.

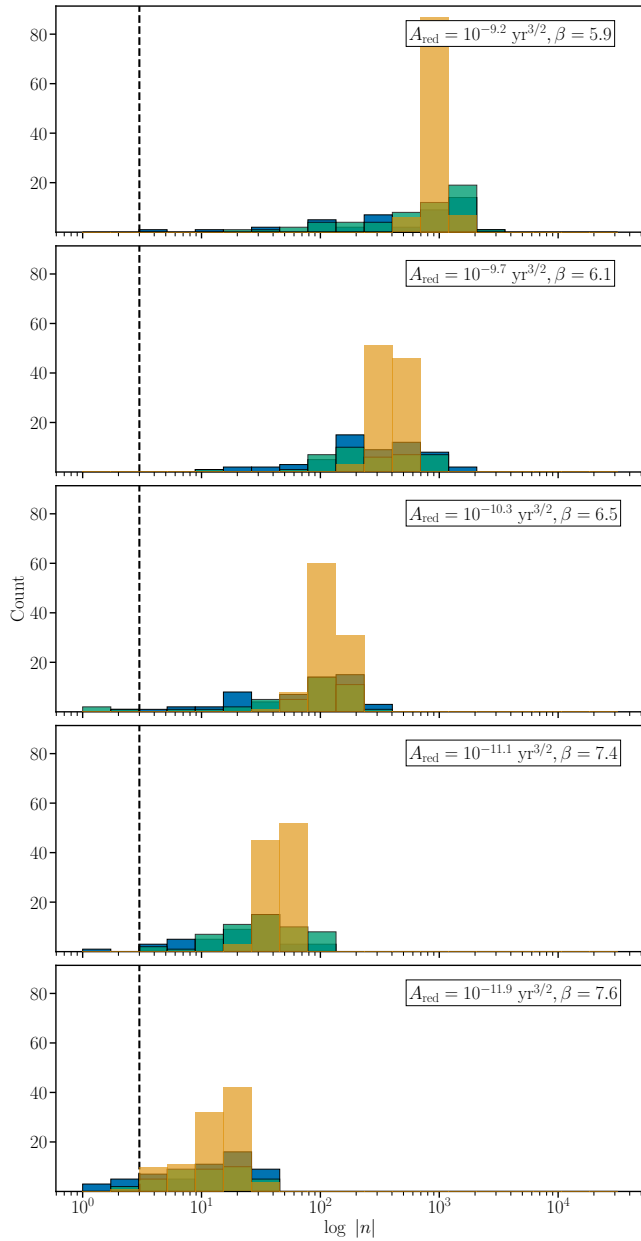


Figure B1. Validation test using the power-law noise model (10) to both generate and analyze the timing data. The format is analogous to Figure 2, viz. distributions of n measurements (blue histograms for $n > 0$, cyan histograms for $n < 0$) and their formal uncertainties Δn (orange histograms) reported by TEMPO2 through (1) and (11) for a representative sample of A_{red} and β values. All panels are constructed from 10^2 random realizations of synthetic data from TEMPO2 and the rotational parameters in Table 2. The black dotted line represents $n_{\text{pl}} = 3$. The averages of n and Δn are 2.9 and 14.7, and -150 and 982.8, for the bottom and top panels, respectively. In the bottom and top panels, the number of measurements satisfying $n - \Delta n \leq n_{\text{pl}} \leq n + \Delta n$ are 55 and 57, respectively. This is in contrast to 41 and 8 measurements for the same panels in Figure 2.